Alma Mater Studiorum · Università di Bologna

Scuola di Scienze
Dipartimento di Fisica e Astronomia
Corso di Laurea Magistrale in Fisica

Study of the track reconstruction in the FOOT experiment for Hadrontherapy

Relatore:
Dott. Marco Selvi

Presentata da:
Riccardo Ridolfi

Correlatore:
Dott. Matteo Franchini

Sessione IV
Anno Accademico 2016/2017

A N., perché sarà solo
una questione di tempo.

Abstract

In Hadrontherapy (also called *Ion Beam Therapy*, IBT) high-energy beams of charged particles (protons and heavier ions) are used against deep tumours: these particles have a lot of advantages with respect to photons used in conventional radiation therapy. Their physical depth-dose distribution in tissue is characterized by a low dose in the entrance channel and a sharp maximum (Bragg peak) near the end of their path, whose depth depends on the beam energy. Moreover, ions heavier than proton, such as Carbon or Oxygen, show an enhanced biological effectiveness in the Bragg peak region, thus allowing a possible treatment of hypoxic tumours. Unfortunately, a major drawback for these ions is the presence of nuclear fragmentation of the projectile, which accounts for a non-zero dose deposited beyond the Bragg peak. In proton treatments, the fragmentation of target nuclei could be an issue instead. A correct assessment of this phenomenon is very important to evaluate the real biological effectiveness of protons. For these reasons the FOOT (FragmentatiOn Of Target) experiment was proposed: its final goal is to measure the heavy fragment ($Z > 2$) cross section with a maximum uncertainty of 5% and the fragment energy spectrum with an energy resolution of the order of $1-2\,\mathrm{MeV/u}$, in order to get a better radiobiological characterization of protons. In this thesis, the determination of the fragment momentum is studied through the track reconstruction in magnetic field, using the Kalman filter technique. In addition, two methods for the proper assignment of hits to the fragment track are developed and discussed.

Sommario

In adroterapia vengono utilizzati fasci di ioni (protoni e ioni carbonio) per il trattamento di tumori profondi; queste particelle possiedono molti vantaggi rispetto ai fotoni utilizzati nella radioterapia convenzionale. Il profilo dose-profondità di questi ioni è caratterizzato da una bassa dose nel canale di entrata e da un massimo molto pronunciato situato alla fine del loro range, chiamato picco di Bragg, la cui profondità dipende dall'energia del fascio. Inoltre gli ioni più pesanti del protone, come il carbonio o l'ossigeno, mostrano un'efficacia biologica maggiore nella regione del picco di Bragg, aprendo così alla possibilità di trattare anche tumori ipossici. Tuttavia il problema più grande nell'utilizzo di questi ioni è la loro frammentazione nucleare che causa una dose non nulla oltre il picco di Bragg. Nei trattamenti con fasci di protoni invece, è la frammentazione del bersaglio ad essere un problema: una conoscenza corretta e approfondita di questo fenomeno sarebbe davvero importante per valutare la reale efficacia biologica dei protoni. L'esperimento FOOT (FragmentatiOn Of Target) è stato proposto proprio per fare luce su questi aspetti: il suo obiettivo finale è quello di misurare la sezione d'urto dei frammenti pesanti, con $Z > 2$, con un'incertezza massima del 5% e il loro spettro energetico con una risoluzione dell'ordine di $1 - 2\,\mathrm{MeV/u}$, così da ottenere una migliore caratterizzazione radiobiologica dei protoni. In questa tesi si intende studiare come si determinano i momenti dei frammenti ricostruendo le loro tracce in campo magnetico usando il filtro di Kalman. Inoltre vengono sviluppati e discussi due algoritmi che hanno lo scopo di assegnare correttamente le hit con le tracce.

Contents

Introduction **4**

1 Motivations for hadrontherapy **6**
1.1 The Physics of Hadrontherapy 11
1.1.1 The Bethe-Bloch formula 11
1.2 Range and Multiple Coulomb Scattering 13
1.3 Nuclear interactions 17
1.3.1 Nuclear fragmentation in heavy ion therapy 19
1.3.2 Nuclear fragmentation in proton therapy 20
1.4 Radiobiology of Ion Beams 22
1.4.1 Absorbed Dose 23
1.4.2 Linear Energy Transfer 25
1.4.3 Relative Biological Effectiveness 26
1.4.4 Oxygen Enhancement Ratio 27

2 The FOOT experiment **30**
2.1 Inverse Kinematics and Cross Sections 32
2.2 Experimental setup 34
2.2.1 The Electronic Detector Setup 34
2.2.2 The Emulsion Spectrometer 38
2.3 Expected performances 40

3 Software and track reconstruction **42**
3.1 Simulation 42
3.2 Reconstruction 44
3.3 Track fitting 45
3.4 Least Squares Method 46
3.5 The Kalman Filter technique 47
3.5.1 State vector and measurement vector 47
3.5.2 Prediction 48
3.5.3 Filtering 49

3.5.4 Smoothing 50
3.6 The Deterministic Annealing Filter 51
3.7 GENFIT 53

4 Interface to the FOOT geometry **55**
4.1 Geometry in FLUKA 55
4.2 Geometry in SHOE 57
4.3 Software updates 59

5 Study of the track reconstruction **60**
5.1 The momentum resolution in the FOOT magnetic spectrometer 60
5.2 Study of the track reconstruction with MC truth 61
5.3 Track finding methods 64
5.4 Minimum distance method 65
5.4.1 Upstream direction 65
5.4.2 Downstream direction 65
5.5 Cylinder method 66

Conclusions and perspectives **72**

Bibliography **73**

Introduction

Cancer is one of the most deathly diseases worldwide: according to the *World Health Organization* Media Centre, cancer accounted for 8.8 million deaths in 2015. In the clinical practice, cancers are treated by surgery, chemotherapy, radiation therapy and, recently, immunotherapy. These techniques could be used alone or combined with each other: for instance, radiation therapy now contributes to the cure of approximately 23% of all cancer patients, used alone (12%) or in combination with surgery (6%) or chemo/immunotherapy (5%). Recent estimates indicate that approximately 50% of all cancer patients could benefit from radiation therapy in the management of their disease, both with curative and palliative purpose. Alongside the well-established radiation therapy with photons, the number of patients treated with charged particle beams is growing in the last decade.

Hadrontherapy (or *Ion Beam Therapy*, IBT) exploits the special behaviour of energy loss of heavy charged particles (protons or heavier ions up to Oxygen) traversing human tissues: indeed, they release little energy just under the skin while they release most of the energy near the end of their path. This sharp peak is called *Bragg peak*. Its depth depends on the beam energy, which is tunable both for cyclotron and synchrotron. In addition, the beam can be moved in the other two directions thanks to sweeping magnets. In this way it is possible to achieve high irradiation accuracy and dose conformity over the tumour volume. Moreover, ions heavier than proton (such as Carbon or Oxygen) show an enhanced biological effectiveness in the Bragg peak region: this feature can be exploited to treat hypoxic tumours and to achieve the same effect with a lower dose.

At present, alongside the correct irradiation of moving organs, a major problem for IBT is the nuclear fragmentation both of the projectile and the target. In heavy ion treatments, the fragments of the projectile (with the same velocity but with lower mass than the projectile itself) can travel farther and can deliver a non-zero dose beyond the Bragg peak, worsening the conformity to the tumour volume. On the contrary, in proton treatments the fragmentation of target nuclei could be an issue, according to several studies. Indeed, such fragments have small ranges ($\sim \mu$m), resulting in a local dose deposition: this effect is more important in the entrance channel, so healthy tissues can be exposed to such a damage.

At present, there is a lack of experimental measurements of nuclear reaction cross

sections for fragments produced in the interaction with tissues nuclei (H, C, Ca, O, N) of $60 - 250\,\mathrm{MeV}$ protons and $100 - 350\,\mathrm{MeV/u}$ Carbon ions, which are the typical energies for IBT. These data will be analized and the results will be integrated in the Treatment Planning Systems, i.e. the software codes used to plan every treatment accounting for the correct dose delivery.

The main goal of the FOOT (FragmentatiOn Of Target) experiment is to measure the target and projectile fragmentation cross sections relevant for IBT. To achieve this goal, the FOOT experiment adopts an inverse kinematics approach to overcome the difficulties to detect particles with a very short range ($\sim \mu$m). In order to circumvent the problems given by the presence of a pure hydrogen target, the subtraction between cross section on C and C_2H_4 is performed. The FOOT apparatus will consists of a start counter, a drift chamber acting as beam monitor, a high precision tracking system in a magnetic field, a time of flight measurement system, and a calorimeter.

The work reported in this thesis has two main goals: firstly, making uniformity between the geometries used by the simulation and the reconstruction framework in order to avoid any compatibility problem. Before this work, the two frameworks did not share neither geometry nor material and compound information. Secondly, we studied the performances of the track reconstruction, especially the reconstructed momenta of the fragments. Moreover, two preliminary track finding methods are developed and compared with true hit assignments provided by Monte Carlo (MC) simulation.

In chapter 1 the basics of charged particles interactions in a medium, including energy loss, multiple scattering and nuclear fragmentation alongside a description of the most important quantities in radiobiology will be introduced. In this chapter the state of the art in IBT is also outlined in order to introduce the rationale behind the FOOT experiment. In chapter 2 the FOOT experimental setup and the strategy for the measurement of short range fragments will be described. In chapter 3 the structure of the simulation and the reconstruction frameworks will be explained, in particular with a detailed description of the Kalman filter technique, included in the open source GENFIT library. In chapter 4 the first original part of this work is presented: in order to make uniformity between the geometry of the simulation and the reconstruction framework, several software updates are described, especially a common definition of the materials in FOOT. In chapter 5 the study of the track reconstruction in the tracking system is performed. Firstly, Monte Carlo truth is used to predict the best achievable result; then, two preliminary track finding methods are explained and their results are also outlined.

Chapter 1

Motivations for hadrontherapy

Cancer is a group of diseases characterized by the uncontrolled growth and spread of abnormal cells. If the spread is not controlled, it can result in death. Although the causes for many cancers, particularly the ones occurring during childhood, remain unknown, established cancer causes include lifestyle (external) factors, such as tobacco use, physical inactivity, exposure to air pollution and excessive body weight. Other internal factors, such as inherited genetic mutations, hormones, and immune conditions are included among cancer causes. These risk factors may act simultaneously or in sequence to initiate and/or promote cancer growth. Several years may often pass between exposure to external factors and cancer occurrence.

According to the *World Health Organization* WHO Media Centre [1], cancer is a leading cause of death worldwide, accounting for 8.8 million deaths in 2015; the most common deathly cancer are cancers of lung, liver, colorectal, stomach and breast. Between $30 - 50\%$ of cancers can currently be prevented. This can be accomplished by avoiding risk factors and implementing existing evidence-based prevention strategies. The cancer burden can also be reduced through early detection of cancer and management of patients. These risk factors combined with the growth and ageing of population, could lead to over 20 million new cancer every year by 2025.

However, it seems to be a decreasing tendency in cancer death rates: according to the last Surveillance Research of the American Cancer Society [2], the female breast cancer death rate declined by 38% from its peak in 1989 to 2014 due to improvements in early detection and treatment. Lung and bronchus cancers confirm themselves as the most lethal cancers in the USA although they had a steep decrease over the last 30 years; however, pancreatic and liver cancers are slightly increasing both in males and females.

The overall improvement in the survival rate is due to both progress in early diagnosis technique and healing technology breakthroughs. Nowadays there are several ways to treat solid tumours: the most known are surgery, chemotherapy, *radiation therapy* (RT) and the newborn immunotherapy. All these techniques can be used alone or combined with each other: for instance, RT now contributes to the cure of approximately

23% of all cancer patients, used alone (12%) or in combination with surgery (6%) or chemo/immunotherapy (5%). Recent estimates indicate that approximately 50% of all cancer patients could benefit from RT in the management of their disease, both with curative and palliative purpose [3].

The roots of RT were established between the 19^{th} and 20^{th} century: the main discovery was Röntgen's in 1895 when he produced X-rays from a vacuum pipe (figure 1.1). His report was followed soon by Becquerel's on the phenomenon of radioactivity and, in 1898, by that of Pierre Curie and Marie Sklodowska Curie on the discovery of radium. Becquerel and Curie reported on the physiologic effects of radium rays in 1901 and since then, such discoveries stimulated speculation that radioactivity could be used to treat disease. Indeed, X-rays were used to treat a patient with breast cancer for the first time in January 1896: these pioneering treatments marked the beginning of RT [4]. Unfortunately, a big issue arose soon: to have an efficient treatment of cancers it is mandatory to deliver radiation only to the tumour mass sparing normal tissues as much as possible[a].

The first application of accelerators in medicine was in 1931, when Ernest Lawrence and Stan Livingston built the first cyclotron. Ernest and his brother John[b] irradiated patients with salivary glands cancer by means of neutron beams produced by 5 MeV accelerated deutons on a beryllium target (figure 1.1); as these neutrons produce nuclear fragments, these treatments can be regarded as the first use of hadrons to cure cancers ever. The groundwork for *hadrontherapy*[c] (also called *Ion Beam Therapy*, IBT) was laid in 1946 when Robert R. Wilson wrote the landmark paper [5] in which he proposed that protons accelerated by machines such as Lawrence's could be used for medical purposes as well as scientific investigations. The first clinical use of a proton beam occurred at Berkeley, California in 1954; limited investigational proton treatment lasted for a few years afterward, until Berkeley scientists, notably Cornelius A. Tobias, a young Hungarian nuclear physicist who collaborated with Lawrence brothers, began investigating biologically damage produced by helium ions. His fundamental research interest was on the effects of ionizing radiation on living cells.

Proton Therapy (PT) began to spread to other physics laboratories around the world. The second use of a physics research accelerator for PT occurred in Uppsala (Sweden) in 1957, while in 1967 beam therapy began at Dubna, USSR. The Japanese experience began in 1979, at Chiba and another facility opened at Tsukuba in 1983. At the Swiss Institute for Nuclear Research (now the Paul Scherrer Institute, PSI), PT began in 1985. The first hospital-based proton facility in the world opened at the Loma Linda University

[a] The term used in clinical practice to indicate a organ which has to be spared by radiation is *Organ At Risk* (OAR).

[b] John Lawrence, a physician, had the idea to treat patients with leukaemia by injecting them with ^{32}P, a isotope of phosphorus which is a β^- emitter, produced with his cyclotron. He is regarded as the founder of nuclear medicine.

[c] The term *hadrontherapy* was coined by Ugo Amaldi in 1992 to collect all non-conventional therapies with proton, ion, pions or neutron beams.

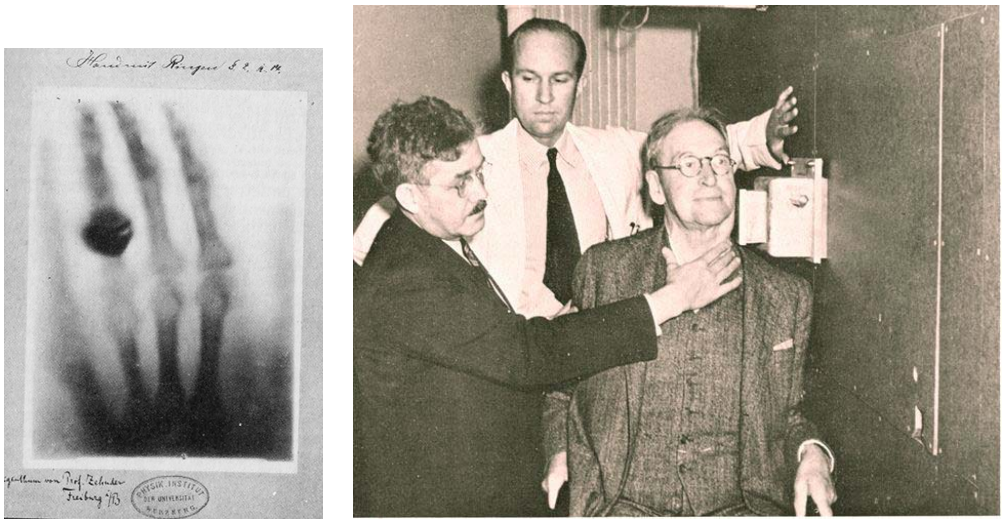

Figure 1.1: The first medical application of X-rays by W. C. Röntgen: the radiography of the hand of his wife (left). Ernest and John Lawrence performed the first salivary gland cancer treatments using one of the first cyclotrons in 1936 (right).

Medical Center (LLUMC) in California and it began to treat patients in 1990 after twenty years of development: here physicists overcame several problems, allowing for the optimal use of protons in cancer therapy. For instance, the first computer-assisted radiation treatment planning was developed here. In those years, the use of several ion beams (such as helium, argon, neon and silicon) and pion beams was investigated to improve clinical results: unfortunately excessive toxicity was observed in patients, especially due to the high dose in the entrance channel of high Z beams. Today proton and carbon ions are used in clinical practice while other interesting ions, such as helium, are going to be used in the next years.

Since 1990, almost 150000 patients have been treated with protons while more than 23000 with carbon or other ions. Up to the end of 2016, there are 72 facilities treating with protons or carbon ions worldwide (Austria, Canada, Czech Republic, China, France, Germany, Italy, Japan, Poland, Russia, South Africa, South Korea, Sweden, Switzerland, United Kingdom, USA) and other 45 facilities are under construction, also in other countries (Belgium, Denmark, United Arab Emirates, India, Netherland, Saudi Arabia, Singapore, Slovakia, Taiwan) [6]. As it can be seen in figure 1.2, IBT accounts only for a small number of all external beam therapy[d] treatments. According to DIRAC (*DIrectory of RAdiotherapy Centres*) database of *International Atomic Energy Agency* IAEA [7], today there are 13880 active external beam therapy facilities: among them, only 80 are proton and carbon ion facilities.

[d]External beam radiotherapy is the most common form of RT: it directs the radiation at the tumour from outside the body.

Figure 1.2: Number of RT centres worldwide divided by equipment type (top). Location of RT centres in the world (bottom).

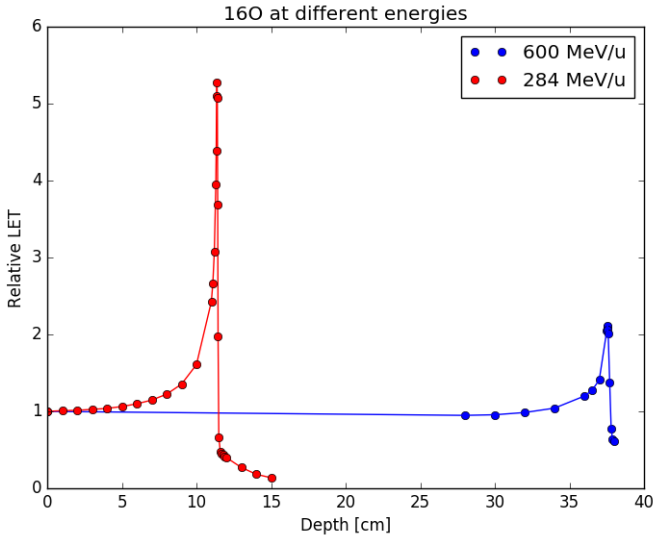

Figure 1.3: Depth-dose profile (Bragg curves) for two oxygen beams of different energy [8].

The main physical advantage of heavy charged particles with respect to photons is their characteristic dose-depth profile. Indeed, while a beam of photons reduces exponentially its intensity with penetration depth, heavy charged particles (protons or heavier ions) lose energy according to Bethe-Bloch law. Their profile is characterized by a low dose in the entrance channel[e] and by a steep rise near the end of their path. This feature makes these particles the best choice to treat deep seated tumours. This special behaviour was firstly described by W. H. Bragg in 1905 for α particles in air and for this reason depth-dose profiles of heavy charged particles are known also as *Bragg curves*. Heavy charged particles are more precise, indeed, but in the clinical practice it can be even advantageous to widen Bragg peaks by passive systems in order to reduce the treatment time: tumour volume is thus covered by several peaks with different energies passed through passive systems. This is the so-called *Spread Out Bragg Peak* (SOBP).

In the first section of this chapter the physical basics of the interaction of heavy charged particles will be summarized. In the second, nuclear interaction between projectile and target will be discussed, notably those of interest for IBT and for the FOOT experiment. In the last, radiobiology and its most important quantities will be introduced, with close attention to the radiobiological differences between RT and IBT.

[e]The first centimetres under the surface crossed by radiation are called *entrance channel*.

1.1 The Physics of Hadrontherapy

Heavy charged particles, such as α particles, interact with matter primarily through Coulomb forces with orbital electrons of absorber atoms. Interactions of the particle with nuclei as in Rutherford scattering are also possible, even if they are less frequent. Upon entering any absorbing medium, the charged particle immediately interacts simultaneously with many electrons. In each interaction, the electron feels an impulse from the attractive Coulomb force as the particle passes its vicinity. Depending on the interaction distance, this impulse may be sufficient either to raise the electron to a higher-lying shell within the absorber atom (*excitation*) or to remove completely the electron from the atom (*ionization*). The energy that is transferred to the electron must come at the expense of the charged particle, and its velocity is therefore decreased as a result of the interaction. The other main process which involves heavy charged particles when entering a medium is the *Multiple Coulomb Scattering* (MCS). It deflects particles from the incident direction without loss of energy. These phenomena will be discussed in the following.

1.1.1 The Bethe-Bloch formula

The linear stopping power S for charged particles in a given absorber is defined as the differential energy loss divided by the corresponding differential path length:

$$S = -\frac{dE}{dx}. \tag{1.1}$$

Its value depends on both the particle and absorber type. The value of $-dE/dx$ along a particle track is also called its *specific energy loss*. This quantity was first calculated by Bohr using classical arguments and later by Bethe, Bloch and others using quantum mechanics. From Bohr's view, let's consider a heavy particle with a charge ze, mass M and velocity v passing through some material medium and suppose that there is an atomic electron at some distance b from the particle trajectory. To perform this calculation three important assumptions have to be made: firstly assume that the electron is free and initially at rest (i.e. its orbital velocity must be much lower than the ion velocity), secondly assume that the latter only moves very slightly during the interaction with the heavy particle so that the electric field acting on the electron may be taken at its initial position. Eventually, assume that the incident particle remains essentially undeviated from its original path because of its much larger mass $M \gg m_e$. Once summing up all contributions from atomic electrons by integrating over the impact parameter b, it's possible to write a expression for the specific energy loss:

$$-\frac{dE}{dx} = \frac{4\pi z^2 e^4}{m_e v^2} N_e \ln \frac{\gamma^2 m_e v^3}{z e^2 \bar{\nu}} \tag{1.2}$$

where $\bar{\nu}$ is the mean orbital frequency of atomic electrons, γ is the Lorentz factor and N_e is the density of electrons. This formula gives a reasonable description of the energy loss for heavy particles such as the α particle or heavier nuclei. However, for lighter particles, like protons, the formula breaks down because of quantum effects.

The correct quantum-mechanical calculation was first performed by Bethe, Bloch and others. In the calculation the energy transfer is parametrized in terms of momentum transfer rather than the impact parameter. The Bethe-Bloch formula can be written as:

$$-\left\langle \frac{dE}{dx} \right\rangle = 2\pi N_a r_e^2 m_e c^2 \rho \frac{Z}{A} \frac{z^2}{\beta^2} \left[ln\left(\frac{2m_e\gamma^2 v^2 W_{\max}}{I^2} \right) - 2\beta^2 - \delta - 2\frac{C}{Z} \right]. \tag{1.3}$$

with

$2\pi N_a r_e^2 m_e c^2 \simeq 0.1535\,\text{MeV cm}^2/\text{g}$
r_e = classical electron radius
m_e = electron mass
N_a = Avogadro's number
Z = atomic number of the medium
A = atomic weight of the medium
ρ = density of the medium
z = charge of the incident particle
$W_{\max}$ = maximum energy transfer in a single collision
I = mean excitation potential
δ = density correction
C = shell correction.

The equation 1.3 is valid if $0.05 < \beta\gamma < 500$ and for particles heavier or equal than the muon ($m_\mu \simeq 106\,\text{MeV}/c^2$). The mean excitation potential, I, is one of the parameters of the Bethe-Bloch formula and it is essentially the average orbital frequency $\bar{\nu}$ from Bohr's formula times Planck's constant; it is theoretically a logarithmic average of ν weighted by the oscillator strengths of the atomic levels [9]. The standard value for water (very similar to the composition of the average human body) is $I \simeq 75\,\text{eV}$ but slightly larger values can be found in literature [10]. The Bethe-Bloch formula has two main corrections: the *density effect* δ and the *shell effect* C/Z. The density effect arises at high energies because the electric field of the particle also tends to polarize the atoms along its path; this polarization shields outer electrons from the electric field so that collisions with these electrons account less to the total energy loss. The shell effect arises at low energies when the speed of the particle is comparable with the speed of orbital electrons: at such energies, the assumption of electron at rest is no longer valid and the

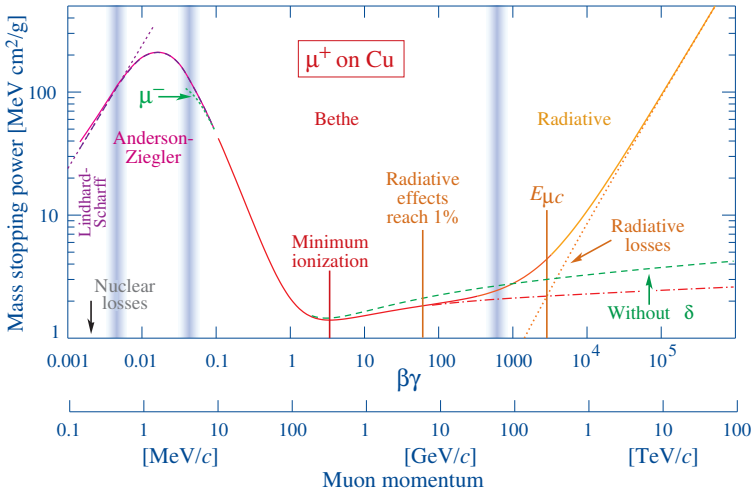

Figure 1.4: Mass stopping power for positive muons in copper as a function of $\beta\gamma = p/Mc$ over nine orders of magnitude in momentum. Solid curves indicate the total stopping power.

equation 1.3 breaks down. Due to the β^{-2} dependence, the energy loss increases with decreasing particle energy until about $v \simeq 0.96c$ (figure 1.4). At low velocities (for light ions below about 10 MeV/u), the effective charge begins to decrease due to the interplay of ionization and recombination processes and Z has to be replaced in equation 1.3 by the effective charge Z_{eff}, which can be described by the empirical formula

$$Z_{\text{eff}} = Z[1 - \exp(-125\beta Z^{-2/3})]. \tag{1.4}$$

Therefore, at the end of the path the electronic stopping power of the projectile drops to zero because of the rapid reduction of its effective charge [11]. The maximum energy loss rate, corresponding to the Bragg peak, is reached at a projectile velocity of

$$v_{\text{BP}} \simeq Z^{2/3} v_0 \tag{1.5}$$

where $v_0 = e^2/\hbar$ is the Bohr velocity and the corresponding β value is 1/137. For carbon ions this maximum occurs at a specific energy of $\simeq 350$ keV/u (figure 1.5). At still lower projectile energies elastic collisions with target nuclei begin to contribute significantly to the energy loss and dominate the stopping process at the very end of the particle path, i.e. in the last few μm. The corresponding dose contribution is, however, very small and can be neglected in RT applications.

1.2 Range and Multiple Coulomb Scattering

The range is the fundamental parameter which characterizes the distal dose fall-off, i.e. the dose deposited along the beam direction. There are different range definitions:

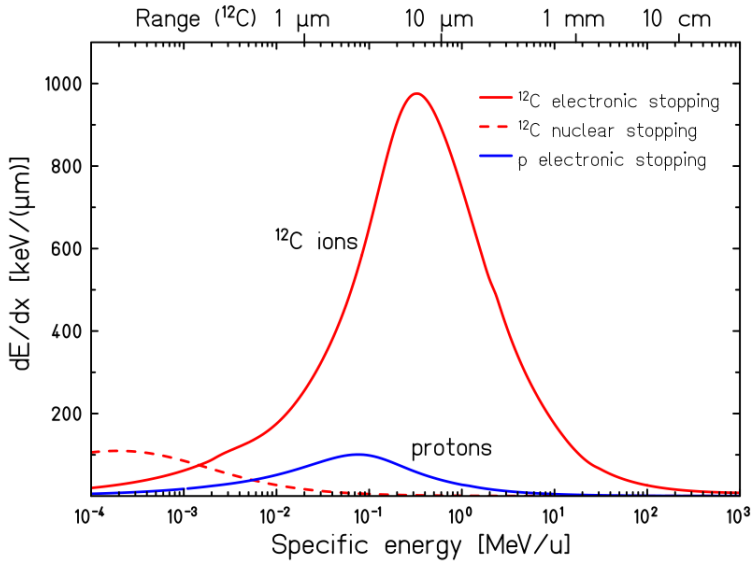

Figure 1.5: Specific energy loss dE/dx of ^{12}C ions and protons in water. The range of ^{12}C ions in water corresponding to their specific energy is indicated at the top.

classical range, mean range, extrapolated range and CSDA (*Continuous Slowing Down Approximation*) range [9]: notably, the latter is a very close approximation to the average path length traveled by a charged particle up to rest position, assuming the rate of energy loss at every point along the track equal to the stopping power at that point. Energy-loss fluctuations, nuclear interactions, δ rays production and Multiple Coulomb Scattering are neglected. The CSDA range is obtained by integrating the reciprocal of the total stopping power (equation 1.3) with respect to energy, that is

$$R(E_0) = \int_0^{E_0} \left(\frac{dE}{dx}\right)^{-1} dE, \tag{1.6}$$

where E_0 is the energy of the incident particle. In IBT treatments one must expect a relation of the type $R \propto E^b$. Indeed, in the β^{-2} region:

$$-\frac{dE}{dx} \propto \beta^{-2} \propto T^{-1}$$

where T is the kinetic energy of the particle. Integrating:

$$R \propto T^2$$

which is consistent with figure 1.6. It is convenient to use kinetic energy instead of total energy because only the former can be lost in the medium in these cases. A more

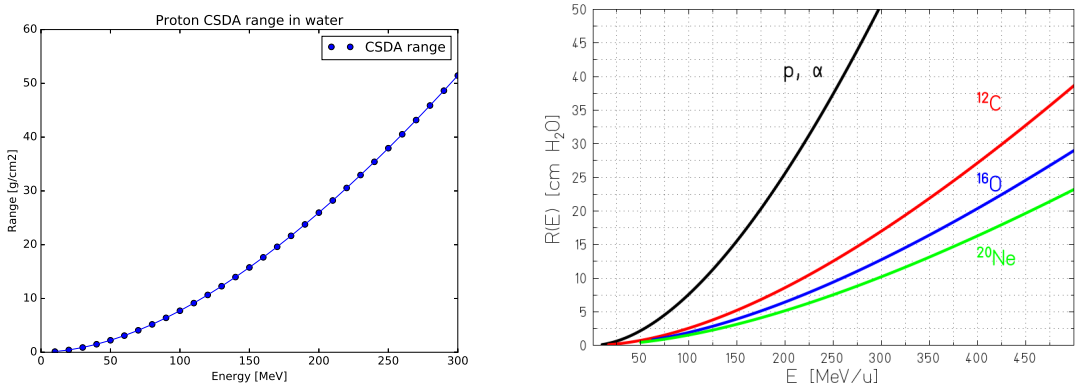

Figure 1.6: CSDA range of protons in water from PSTAR tables [12] (left). Mean range of heavy ions in water (right).

accurate fit in the energy range of interest for IBT leads to $1.7 \lesssim b \lesssim 1.8$ for protons [11].

According to equation 1.6, the energy loss of a single proton plotted as a function of absorber depth would result in a very sharp peak near the stopping point; however, statistical fluctuations of the energy loss in the large number of collisions of the slowing-down process result in a broadening for a ion beam consisting of many particles. These fluctuations are described by the asymmetric Vavilov distribution for charged particles passing through a thin layer of matter, the so-called *energy-loss straggling*. For relatively thick absorbers such that the number of collisions is large, the energy loss distribution becomes a Gaussian [f]:

$$f(x, \Delta) = \frac{1}{\sqrt{2\pi\sigma_E}} \exp \frac{(\Delta - \bar{\Delta})^2}{2\sigma_E^2} \tag{1.7}$$

with x thickness of absorber, Δ energy loss in the absorber, $\bar{\Delta}$ mean energy loss, σ standard deviation. The latter can be written as:

$$\sigma_E = 4\pi Z_{\text{eff}} Z e^4 N_a x \frac{1 - \beta^2/2}{1 - \beta^2}. \tag{1.8}$$

The variance σ_R^2 of the range straggling is related to the variance σ_E^2 of the energy-loss straggling by

$$\sigma_R^2 = \int_0^{E_i} \left(\frac{d\sigma_E}{dx}\right) \left(\frac{dE}{dx}\right)^{-3} dE. \tag{1.9}$$

[f]This follows directly from the Central Limit Theorem in statistics which states that the sum of N random variables, all following the same statistical distribution, approaches that of a Gaussian-distributed variable in the limit $N \to +\infty$.

The ratio of the straggling width σ_R and mean range R is nearly constant and can be described by

$$\frac{\sigma_R}{R} = \frac{1}{\sqrt{M}} f(\gamma) \tag{1.10}$$

where f is a slowly varying empirical function depending on the absorber and γ is the Lorentz factor for the incident particle. For light ions in water the relative straggling σ_R/R is of the order of 10^{-3}. Because of the $1/\sqrt{M}$ dependence, the Bragg peak is sharper for heavier ions than for protons.

Another main process involving charged particles traversing a medium is *Multiple Coulomb Scattering* (MCS). A charged particle traversing matter will be scattered by the Coulomb potentials of nuclei and electrons. In contrast to the ionization energy loss which is caused by collisions with atomic electrons, multiple scattering processes are dominated by deflections in the Coulomb field of nuclei. This leads to a large number of elastic scattering processes with very low deviations from the original path. The distribution of scattering angles due to MCS is described by Molière's theory. For small scattering angles the higher-order terms in Molière's solution can be neglected and the angular distribution can be approximated by a Gaussian function centred in $\theta = 0$ with a standard deviation given by

$$\sigma_\theta = \frac{13.6\,\mathrm{MeV}}{\beta pc} z \sqrt{\frac{x}{X_0}} \left[1 + \frac{1}{9} \log_{10}\left(\frac{x}{X_0}\right)\right] \tag{1.11}$$

where p is the momentum, βc the velocity, and z the charge of incident particle. x/X_0 is the thickness of scattering medium measured in units of radiation length

$$X_0 = \frac{A}{4\alpha N_a Z^2 r_e^2 \ln\left(183 Z^{-1/3}\right)} \tag{1.12}$$

which clearly depends only on scattering medium (for water $X_0 \simeq 36\,\mathrm{g/cm^2}$). Larger scattering angles caused by collisions of charged particles with nuclei are, however, more frequent than expected from a Gaussian distribution so that the final distribution is characterized by long tails which are not consistent with a single Gaussian hypothesis [13]. Several parametrizations to evaluate MCS distribution, notably its tails experimentally generated by nuclear interactions are used to speed up calculations in order to improve treatment accuracy.

In figure 1.7 MCS for ^{12}C ions and protons in a typical treatment beam line can be compared. The angular spread for heavy charged particles is small but increases towards low energies, according to the denominator in equation 1.11; comparing beams with the same range in water (i.e. 150 MeV protons and 285 MeV/u ^{12}C ions with $R = 15.6\,\mathrm{cm}$) shows that σ_θ for protons is more than three times larger than that for carbon ions. This feature makes these ions suitable for treating cancers nearby organs at risk; unfortunately, carbon ion fragmentation at this energy (see later) results in a non-zero dose beyond the

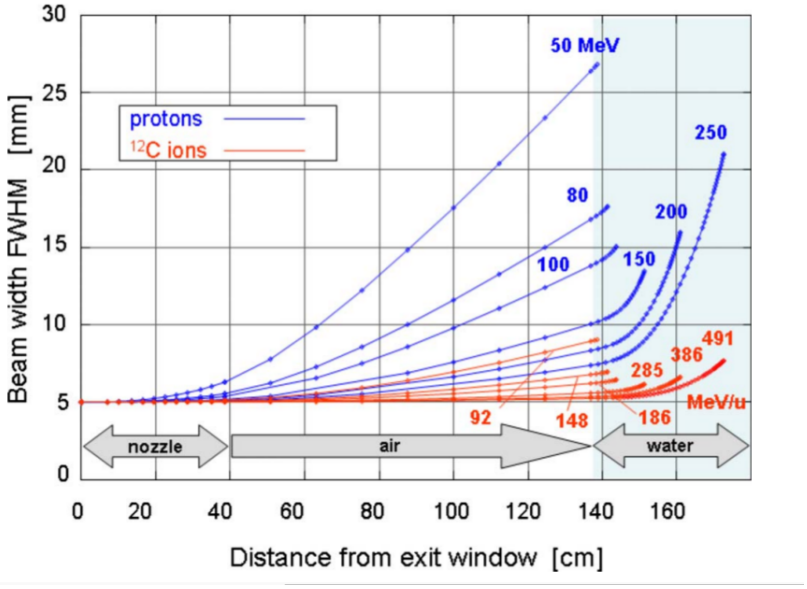

Figure 1.7: Calculated beam spread for ^{12}C ions and protons in a typical treatment beam line with a initial 5 mm FWHM.

Bragg peak which can be dangerous for normal tissue behind the tumour volume. For this reason, investigations on intermediate ions such as helium, lithium and beryllium have been performed in recent years.

1.3 Nuclear interactions

While inelastic collisions between high-energy heavy ions and atomic electrons are very frequent, the probability of nuclear reactions is much smaller but leads to significant effects at large penetration depths. The most frequently occurring nuclear reactions are peripheral collisions where the beam particles may lose one or several nucleons. This process can be described by the abrasion–ablation model [14] as illustrated in figure 1.8. Nucleons in the overlapping zone between the interacting projectile and the target nucleus are "abraded" and form a hot reaction zone (fireball), whereas the outer nucleons (spectators) are only slightly affected by the collision. The fireball is treated relativistically as an ideal gas whose temperature is determined by the available energy per nucleon [15]. In the second step (ablation), the remaining projectile and target fragments as well as the fireball de-excite by evaporating nucleons and light clusters. Those emitted from the projectile fragments appear forward peaked in the laboratory frame due to the high initial velocity of the projectile. The projectile fragments continue travelling with nearly the same velocity and direction as the projectile itself, and contribute to the dose de-

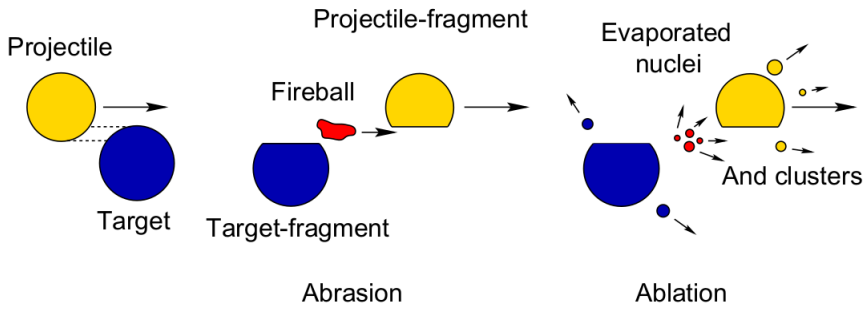

Figure 1.8: Illustration of abrasion-ablation model of peripheral collisions at high energies [16].

position until they are completely slowed down or undergo further nuclear reactions. Neutrons and clusters from target fragments are emitted isotropically and with much lower velocities. Nuclear fragmentation reactions lead to an attenuation of the primary beam flux and a build-up of lower-Z fragments with increasing penetration depth. The lower-Z fragments have longer ranges than the primary ions as the range of particles (at the same velocity) scales with A/Z^2. Therefore, the depth-dose profile of heavy-ion beams shows a characteristic fragment-induced tail beyond the Bragg peak [16].

The main goal of the FOOT experiment is indeed to measure different nuclear fragmentation cross sections relevant for IBT, both of target and projectile.

According to the exponential law, starting with an initial number of particles N_0 which traverse a medium with thickness x, the expected number of particles which had no interactions can be calculated as follows:

$$N(x) = N_0 \exp\left(-x/\lambda\right) \tag{1.13}$$

where λ is the *mean free path* for a given total reaction cross section σ_R and it can be written as

$$\lambda = \frac{M_{\text{mol}}}{N_a \rho \sigma_R} \tag{1.14}$$

where M_{mol} and ρ are molecular mass and density of the crossed medium, respectively. Notwithstanding that theoretical knowledge of these fragmentation processes is poor, several reaction cross sections have been measured in these decades and parametrizations are available, too. Notably, the Bradt-Peters equation is considered to be a good parametrization [17]:

$$\sigma_R = \pi r_0^2 c_1(E) \left[A_p^{1/3} + A_t^{1/3} - c_2(E)\right]^2 \tag{1.15}$$

where A_p and A_t are mass number of projectile and target, respectively, r_0, c_1 and c_2 are parameters depending on the model. Nuclear fragmentation is a high-priority issue for any future development in IBT field. In fact, Monte Carlo codes for medical

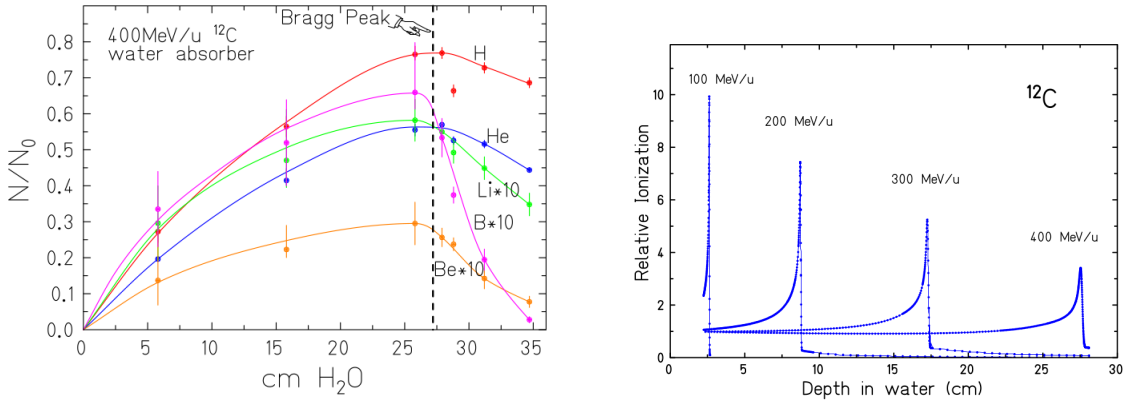

Figure 1.9: Buildup of secondary fragments produced by 400 MeV/u ^{12}C ions stopping in water (left). Measured Bragg curves of ^{12}C ions stopping in water (right).

purpose make use of reaction cross section as input parameters in order to calculate the probability of nuclear interactions but any uncertainty affecting these values propagates in the calculations and thus affects the accuracy of final results.

1.3.1 Nuclear fragmentation in heavy ion therapy

High-energy fragmentation reactions occurring along the beam penetration path in tissue lead to attenuation of the primary beam flux and build-up of secondary lower-charge fragments which give rise to the characteristic dose tail behind the Bragg peak. These effects become most significant at large initial energy and correspondingly large penetration depth of the primary beam [18]. As an example, measured build-up curves for charged fragments of primary ^{12}C ions with $Z = 1$ to 5 are shown on the left of figure 1.9: hydrogen and helium fragments are the most abundantly produced. The heavier fragments like boron are slowed down shortly after the Bragg peak, while hydrogen and helium fragments with much longer ranges (considering that $R \propto T^2$, $T = p^2/2m$ and, as fragments have roughly the same momentum of parents, $R \propto 1/m^2$) produce the longer part of dose tail.

In figure 1.9 (left) the impact of nuclear fragmentation on the depth-dose profile is shown, too [19]. With increasing penetration depth the peak-to-entrance dose ratio[g] becomes gradually smaller, mainly caused by the exponential flux reduction of primary ions (equation 1.13). The buildup of lower-Z fragments is clearly visible in the dose tail behind the Bragg peak at larger depths: this is the main issue of heavy ion therapy, especially in the vicinity of OAR.

[g]The *peak-to-entrance* ratio is the ratio between the dose value at the Bragg peak and the dose value at the entrance channel.

Ion	E [MeV/u]	σ_R (mb)	λ (cm)
p	200	352	85.2
^{4}He	200	767	38.6
^{12}C	380	1424	20.8
^{20}Ne	530	1929	15.5

Table 1.1: Total reaction cross section σ_R and mean free path in water λ of high-energy ions with about 25 cm range in water [20].

1.3.2 Nuclear fragmentation in proton therapy

Differently from heavy ions, protons cannot fragment at the treatment energy so that the produced fragments are only those of the target nuclei. Taking the mean free path of proton in water from table 1.1 and recalling equation 1.13, it is possible to evaluate the nuclear interaction rate for a therapeutic proton beam. Thus, approximately 1% of protons interact with nuclei in a centimetre of tissue [21]. An expected average energy of recoil fragments can be calculated with the Goldhaber formula [22]

$$E_f = \frac{3}{5}\frac{p_F^2}{2m_0}\left(\frac{A_t - A_f}{A_t - 1}\right) \tag{1.16}$$

where A_t and A_f are the target and fragment mass, respectively, m_0 is the proton rest mass and p_F is the Fermi momentum. The dependence of p_F on the fragment mass has been investigated and its best fit leads to the empirical equation [23]

$$p_F = 281\text{MeV/c} \cdot (1 - A_f^{-0.568}). \tag{1.17}$$

Thus, equations 1.16 and 1.17 show that, for a given target material, the average fragment energy will be higher for light fragments. Moreover, the expected average energy of the produced fragments is higher with increasing target mass.

Target fragmentation seems to be very important under several aspects of clinical relevance: indeed, secondary fragments contribute to the overall dose deposited in the patient and those fragments with low energy and/or high-Z show also a higher biological effectiveness, hence a higher damage. In figure 1.10 the fraction of 250 MeV protons surviving at several depths in water is plotted. Here, it can be appreciated that only about 60% of primary protons reach the Bragg peak region. At the same time, the reaction cross section has an almost constant value in the entrance channel but it shows a steep rise in the last $8-10$ cm of range. Eventually, if a cell is considered dead when hit by a single fragment, about 10% of the biological effect induced in the entrance channel might be associated with target fragments while they account only for a 2% of overall damage in the Bragg peak. In [21] it appears that light fragments could have enough

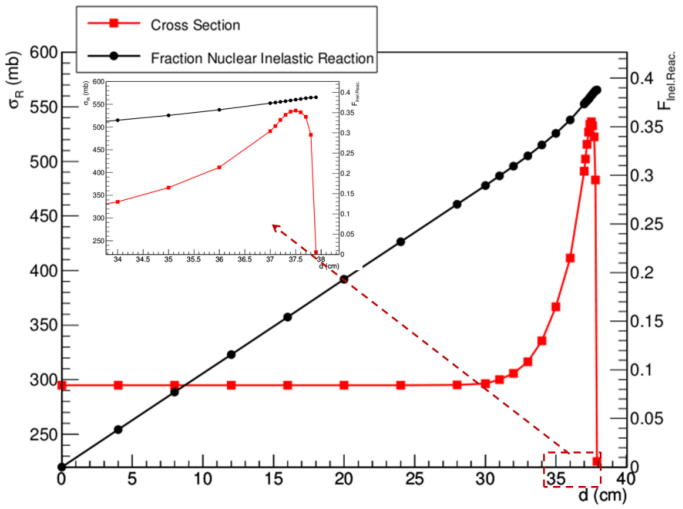

Figure 1.10: Fraction of nuclear inelastic reactions and total reaction cross section for a 250 MeV proton beam in a water target as a function of path length. The total reaction cross section is calculated with data currently used in *Treatment Planning System* (TPS). The inset shows a zoom of the last centimetres of range.

energy to hit more than a single cell: in fact the diameter of a red blood cell is $\simeq 8\,\mu m$, that of a skin cell $\simeq 30\,\mu m$ while the range of a 2.5 MeV deuton can reach $\simeq 70\,\mu m$.

In [24] the contribution of secondary particles to pencil and passively scattered 160 MeV proton beams is investigated. Notably, more than 99.9% of absorbed dose is given by primary and secondary protons, α particles and heavy secondaries. In the entrance region before the Bragg peak approximately 90% of the total dose is given by the primary protons, with a steep decrease in the Bragg peak; the secondary protons account for up to 8% of the dose release in the entrance region, their contribution decreases in the Bragg peak but it increases beyond the Bragg peak due to their forward peaked emission.

As already emphasized, the contribution of secondary particles produced in nuclear fragmentations of target cannot be considered negligible anymore. In figure 1.11 it is possible to compare the number of cells killed by a target fragment (red dots) and those killed by a ionization of a primary proton, assuming the death of each cell in which a fragmentation occurs. Both the cell killing contributions increase in the Bragg peak region, but the effect due to ionisation of primary protons is boosted with respect to that of nuclear fragmentation. On the contrary, in the entrance channel the predicted survival is high and the contribution of secondaries is more relevant.

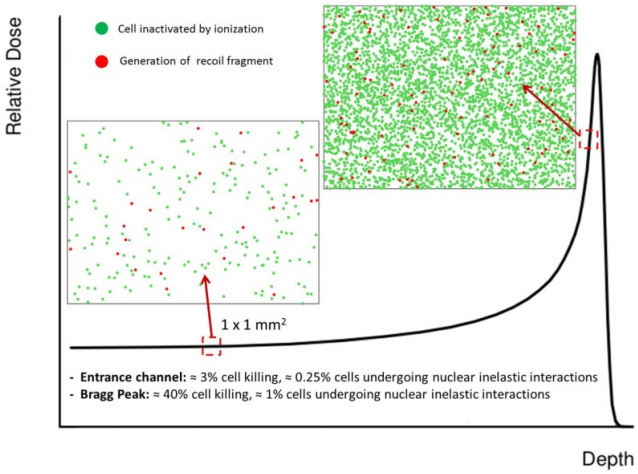

Figure 1.11: The figure schematically shows the impact of ionization and target fragmentation in tissue sections of $1 \times 1\,\mathrm{mm}^2$. The effect is considered at two different positions along the depth-dose profile. Even though both the contributions of ionization and fragmentation increase when approaching the Bragg peak, at that position the biological effect is mainly due to ionization events. On the contrary, in the entrance channel the predicted survival is high, and therefore a significant role might be played by low-energy target fragments.

1.4 Radiobiology of Ion Beams

Biological effects after exposure to ionizing radiations proceed in a precise time sequence which spans several orders of magnitude in time. The first step is the *physical* process, such as energy absorption by the atoms and molecules, in less than $10^{-15}\,s$ after the irradiation. The second step is the so called *chemical* process, meaning that the reaction drives direct or indirect molecular changes including free-radical production (in the order of $10^{-6}\,s$) and eventually *biological* processes may occur. Here biological effects such as damages to biomolecules in the cell components (i.e. DNAs, proteins) in the order of $10^{-3}\,s$ are included. A fraction of those damages will be repaired through biological processes of healthy cells. If the DNA damage cannot be repaired, the cell may die (apoptosis) or it can become unable to duplicate. Damaged healthy cells could also survive and reproduce with a mutated DNA which could become a trigger to cell mutations or tumours [25].

Biological effects due to radiation exposure are divided into two categories, *direct* and *indirect* action (figure 1.12). DNA molecules can receive energy directly from the secondary electrons produced by the incident radiation, resulting in their ionization, and are damaged by the breakage of their chemical bonds. This direct action of radiation accounts for approximately 1/3 of all biological effects caused by ion irradiation. DNA molecules can also be damaged by active group of molecules (free radicals) produced by ionization of the surrounding water molecules. This is an indirect action of radiation

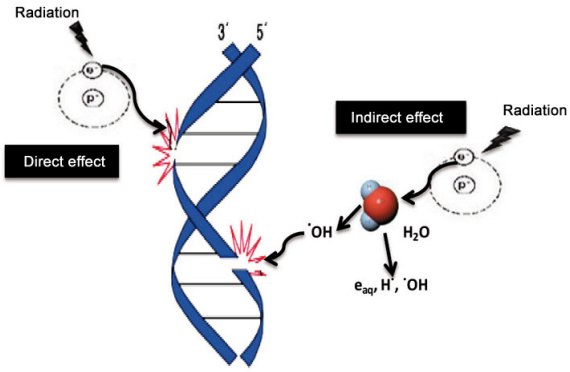

Figure 1.12: Direct and indirect actions of radiation. The structure of DNA is shown schematically.

and accounts for the remaining 2/3 of the biological effects [26]. The indirect action mainly consists of the chemical reactions of water molecules with the body constituents and can be affected by various surrounding free-radical collectors. Free-radicals deprive a biomacromolecule (R) of a hydrogen atom (dehydrogenation) to make a radical R; the radical R binds with a hydroxyl radical (OH·) or reacts with another radical biomolecule to compose a new molecule, damaging in this way the cell functionality.

DNA damages can be mainly of two types: *Single Strand Breaks* (SSB) and *Double Strand Breaks* (DSB). Both can be repaired by DNA polymerases[h] but DSB are much more difficult to repair, especially if they occur in clusters. In the following, the main radiobiological quantities will be described and discussed.

1.4.1 Absorbed Dose

The most important physical quantity in radiotherapy is the dose deposited in tissue. It is defined as the mean energy dE deposited by the ionizing radiation in a mass element dm:

$$D = \frac{dE}{dm} \tag{1.18}$$

which is measured in *Gray* [Gy] where $1\,\mathrm{Gy} = 1\,\mathrm{J/kg}$. In order to quantitatively describe the properties of radiobiological effects using survival curves[i], several models have been

[h]DNA polymerases are enzymes that synthesize DNA molecules from deoxyribonucleotides, the building blocks of DNA. These enzymes are essential for DNA replication and usually work in pairs to create two identical DNA strands from a single original DNA molecule. During this process, DNA polymerase reads the existing DNA strands to create two new strands that match the existing ones.

[i]A cell *survival curve* is a curve used in radiobiology. It depicts the relationship between the fraction of cells retaining their reproductive integrity and the absorbed dose of radiation. Conventionally, the

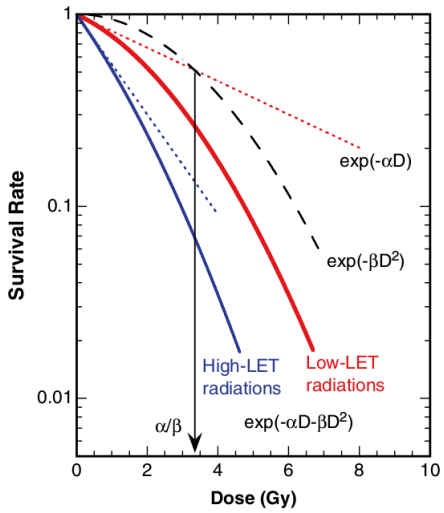

Figure 1.13: Survival curves and parameters in the Linear Quadratic model. Overall cell survival curves (solid lines) for low and high-LET radiations are plotted with each component in the LQ equations as the linear components (dotted lines) and quadratic components (broken line). The dose of the crossing points indicates the α/β-value. Survival curve for high-LET radiation is drawn under the assumption of 3 times higher α-value with the same β-value to the low-LET radiation.

proposed. One of these is the so called *target theory* in which three assumptions have to be made: firstly, only few parts of a cell are sensitive to ionizing radiations and regarded as targets for radiations; secondly, the targets are much smaller than the entire cell but essential for survival of the cell. The last assumption can be summarized as "all or nothing": when sensitive targets are hit by radiations, the cell loses its functions to become inactivated (killed). The Linear Quadratic model, used in figure 1.13, has replaced target theory in modern dose calculation tools.

This model takes into account the different effects between SSB and DSB: the former doesn't cause a lethal damage while the latter could. The probability for a radiation track to cause a SSB is proportional to the first-order term of the dose; although the first ionizing event breaks one strand of DNA but does not lead to inactivation of the cell, the second event cleaves another strand leading to inactivation: the probability of this composite event is proportional to square of the dose. Considering these two causes, the radiation effect on a cell population can be expressed as the *survival probability* $S(D) = \exp(-\alpha D - \beta D^2)$, where two constants α and β have been introduced and D is the dose [25].

Notably, α shows the intrinsic cell radiosensitivity and it is the natural logarithm

surviving fraction is depicted on a logarithmic scale, and it is plotted on the y axis against dose on the x axis.

of the proportion of cells that die or will die due to their inability to repair radiation-induced damage per Gy of ionizing radiation, while β reflects cell repair mechanisms and it is the natural logarithm of the proportion of repairable cells due to their ability to repair the radiation-induced damage per Gy of ionizing radiation. While α-value is more important for high-LET radiations, β-value is more important for low-LET ones. Eventually, the highlighted quantity in figure 1.13 α/β is the value assumed by the absorbed dose for which the number of acutely responding cell deaths is equal to the number of late responding cell deaths (i.e. the dose for which the linear and quadratic components of cell death are equal). This quantity assumes different values according to the type of tissue considered [27].

Experimental data agree with LQ model over a wide range of dose and tissues: unfortunately, LQ model does not take into account treatment time and dose rate.

1.4.2 Linear Energy Transfer

The *Linear Energy Transfer* (LET) is a measure of the energy deposited by an ionizing particle traveling through matter. It is closely related to the stopping power described in subsection 1.1.1 and it is defined as the ratio between the energy deposited dE by a particle in a track element with length dl:

$$\mathrm{LET}_\delta = \left(\frac{dE}{dl}\right)_\delta \tag{1.19}$$

which is measured in keV/μm. Here δ is an upper threshold for the energy of secondary emitted electrons which has been introduced in order to consider only those electrons which deposit energy locally excluding those which have a longer path. While stopping power can be seen as a material property which describes the energy absorbed by matter, LET describes the energy loss of the particle. If all the secondary electron energies are considered ($\delta \to W_{\max}$), LET, numerically, equals stopping power [28].

LET has long been viewed as a major parameter to quantify biological effects of radiations. It is not a constant value as it changes with the projectile energy, yielding to the characteristic Bragg peak shape described before in Sec. 1.1.1.

Even though LET is not a good parameter to describe the full spectrum of biological radiation effects, it is still a widely used quantity to categorize ion-induced damage. In figure 1.13 difference between high and low-LET radiations can be appreciated. Given a cell survival rate, high-LET radiations deliver less dose with respect to low-LET ones. For patients, this reduces the probability of side effects, like secondary cancers, and it can avoid toxicity of normal tissues.

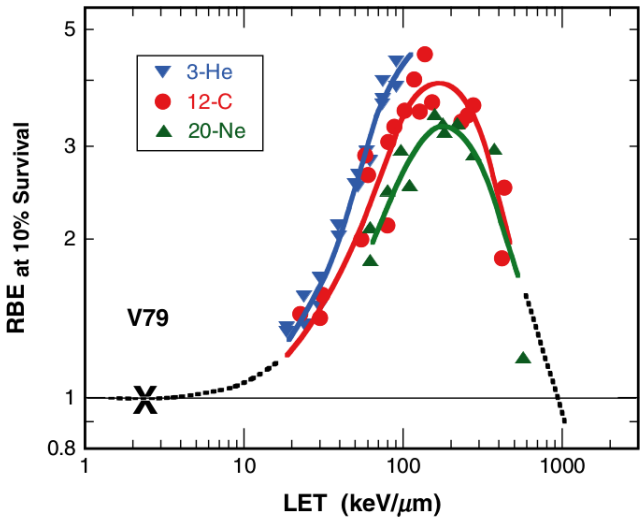

Figure 1.14: RBE to different LETs for different ion species for cell killing of V79 Chinese hamster cells [29].

1.4.3 Relative Biological Effectiveness

The biological effect depends on the quality of the delivered radiations. According to the LET, X-rays, or γ-rays up to several keV/μm can be classified into low-LET radiations, while hadron beams with tens of keV/μm or more are classified into high-LET radiations. However, it is mandatory to find other quantities to describe biological effects: one of these is the *Relative Biological Effectiveness* (RBE), which is used to compare different particle effects on biological tissues.

It is defined as the ratio of the dose of a reference radiation (typically 250 keV X-rays) to the dose of the radiation under test (ions, for instance) in order to produce an identical biological effect (isoeffect) by both:

$$\mathrm{RBE}_{\mathrm{iso}} = \frac{D_{\mathrm{ref}}}{D_{\mathrm{test}}}. \tag{1.20}$$

It is worth pointing out that RBE requires both the specification of the reference radiation and the level of biological effect and one must pay attention to avoid misunderstanding. Indeed, RBE is a quantity of paramount importance in clinical practice because it represents the conversion between the absorbed (physical) dose of equation 1.18 and the biological dose, i.e. the so called photon-equivalent dose.

RBE has several known dependecies which have been under investigation in the last decades. Firstly, RBE depends on LET but not linearly as one can expect. As a matter of fact, RBE for ions seems to increase with increasing LET but, after a maximum placed approximately at 100 keV/μm, RBE decreases rapidly (figure 1.14). This is the so called

overkill effect: at a certain LET value, the dose deposition per unit length is so large that the passage of a single particle sufficiently reduces cell survival probability. In this case, the additional dose deposited by ions with a higher LET is wasted and this effect would account for a plateau in RBE over LET plot. In order to justify the decrease of RBE, one has to consider that the number of ions required for the same dose deposition is lower for particles with higher LET so that the ratio of cells without any particle hit increases resulting in a lower RBE for cell killing [30].

Secondly, the particle type influences the position of RBE maximum: notably, for heavier particles the maximum in RBE over LET plot shifts to higher energies. This effect can be explained comparing carbon ions and protons at the same LET, for instance. At the LET corresponding to the RBE maximum for protons, carbon ions are much faster than protons resulting in broader tracks with a reduced ionization density in the track center, therefore at the same LET the biological damage of carbon ions is smaller than protons. In order to achieve the maximum RBE, slower ions (i.e. smaller track size) and higher LET are required.

Eventually, RBE depends also on biological endpoint and on radiosensitivity of the irradiated tissue. For mammalian cells which show radioresistance to conventional radiation, RBE for carbon ions assumes high values while for other photon-sensitive cells (e.g. Chinese Hamster Ovary, CHO) RBE keeps small values.

The value of maximum RBE is not fortuitous: at that density of ionization, the average separation between ionizing events almost coincides with the diameter of the DNA double helix (2 nm). Radiation with this density of ionization has the highest probability of causing a DSB by the passage of a single charged particle, and DSBs are the basis of most biologic effects [31]. Moreover, the ionization cross section in water of secondary electrons produced around the track exhibits its maximum at about 100 eV which corresponds to a mean free path of a few nanometres [32]. Strictly speaking, there is also a high probability for secondary electrons to produce a DSB through two consecutive ionization events.

1.4.4 Oxygen Enhancement Ratio

In RT, the treatment of hypoxic tumours creates a specific challenge: when cancers are growing in size, new blood vessels need to be created in order to supply oxygen to the cells of tumour core. However, these vessels are often generated slowly or with poor quality[j]: therefore, the oxygen concentration inside the tumour is low and there are often regions with a pressure less than 5 mmHg in large size tumours with respect to normal values up to 80 mmHg. The presence of oxygen allows the production of the reactive hydroperoxyl radical $HO_2\cdot$, enhancing the effectiveness of indirect radiation damage. Therefore, a hypoxic region is characterized by a large radioresistance which

[j] In clinical practice, these are called effects of *poor angiogenesis*.

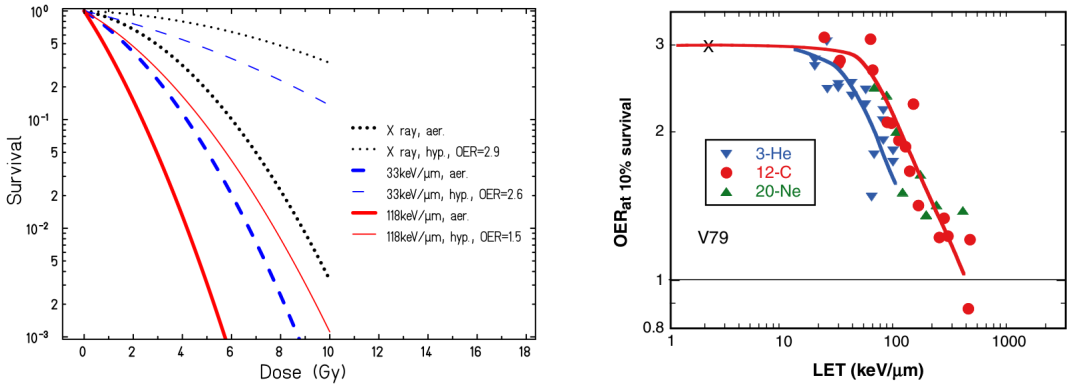

Figure 1.15: Influence of the oxygen level on cells of human kidney T-1 cells for carbon ions with different LET (left). OER to different LETs for different species for cell killing of V79 Chinese hamster cells [30, 29].

is a big issue in treatment planning because a larger dose delivered to the tumour mass means a larger dose to normal tissues, too.

This oxygen effect is quantified by the *Oxygen Enhancement Ratio* (OER):

$$\mathrm{OER} = \frac{D_{\mathrm{hypoxic}}}{D_{\mathrm{aerobic}}}, \tag{1.21}$$

where D_{hypoxic} and D_{aerobic} are the doses in hypoxic and non-hypoxic conditions, respectively, resulting in the same biological effect.

Contrary of RBE, OER is independent on the dose but depends on LET. Generally, OER is about 3 for conventional radiation, while it is significantly reduced for ions for which the direct damage is greater. As it can be seen in figure 1.15, hypoxic and aerobic conditions are similar for high-LET particles (red lines), while they appear very different for low-LET particles (blue and black lines).

In the same figure on the right it is possible to deduce that OER decreases with decreasing particle energy and for high-LET it is close to 1. Cell survival studies has been carried out since 1970s and it was found that the minimum OER is lower for heavier ions such as carbon or neon than for helium: the higher radiation damage of ions by means of direct action instead of free radicals reduces the oxygen effect.

Despite heavier ions such as neon has a OER close to 1 and a higher RBE in the Bragg peak, their use is discouraged because of high dose in the entrance channel, which reduces drastically the peak to entrance ratio, and also because of large nuclear fragmentation. The choice of the most suitable ion is a delicate compromise among all these aspects.

At the moment a constant value of 1.1 for RBE of protons is considered: however, the results presented in the section 1.3.2 give several indications to consider a variable value. Therefore, it is mandatory to improve the knowledge about nuclear fragmentation in PT.

A more complete RBE model, which takes into account nuclear fragmentation, could be very important in order to reduce the dose delivered to healthy tissues. The FOOT (FragmentatiOn Of Target) experiment will provide several cross section measurements relevant for hadrontherapy. The details of this experiment will be presented in the next chapter.

Chapter 2

The FOOT experiment

The main goal of the FOOT (*FragmentatiOn Of Target*) experiment is the measurement of target and projectile fragmentation cross sections relevant for IBT. These results are of primary importance in order to improve knowledge about nuclear interactions taking place in the patient and in order to account for fragmentation effect during the treatment planning. Nowadays there is a lack of experimental data of nuclear reaction cross sections in the energy range of therapeutic application (using as projectile $50 - 250$ MeV protons over C, N, O and $50 - 400$ MeV/u carbon ions over H, C, N, O nuclei) such that only simulation models are used. Nuclear cross sections are critical inputs for these simulation frameworks and these experimental data are necessary to benchmark the Monte Carlo codes for their use in IBT.

Firstly, FOOT will be able to measure target fragmentation in proton treatments: as seen in subsection 1.3.2, the target fragment spectra are extremely peaked to very low energies so that particles can travel only for distances shorter than $100\,\mu$m preventing any detection. This difficulty is overcome by using a inverse kinematic approach. In order to obtain these data, 200 MeV/u ^{12}C and ^{16}O beams over C and C_2H_4 targets will be used. The procedure will be detailed in the next section.

Secondly, FOOT will be able to provide other data from direct kinematic approach about projectile fragmentation in IBT, notably with carbon, oxygen and helium ions [33]. As seen in subsection 1.3.1, carbon ions fragmentation generate a non-zero dose beyond the Bragg peak, such that they are not suitable to treat cancers just in front of OARs. Notwithstanding this drawback, carbon ions suffer from a small lateral deflection and they have a narrow Bragg peak which allow a more precise treatment than with protons, and an enhanced RBE in the SOBP. It is necessary to know fragmentation features very well in order to use it effectively. Oxygen beams are increasingly considered as a fundamental tool against hypoxic tumours: since in figure 1.15 it has been shown that OER steeply decreases with LET, especially beyond $100\,\mathrm{keV}/\mu$m, the rationale for using oxygen beams is basically driven by their similar characteristics with respect to carbon, but with a larger LET distribution on target which is very effective to treat hypoxic

regions. However, in aerobic conditions, the use of oxygen ions is discouraged because of larger fragmentation and small peak to entrance ratio: in clinical practice, oxygen beams could be used to boost the treatment at the end. Helium beams are regarded as a promising alternative to protons instead, both for their cost/benefit ratio and for the reduced impact of MCS on them (equation 1.11). The latter feature allows a higher precision in lateral direction such that OARs can be easily spared. Moreover, RBE for helium seems to be greater than 1 so that biological effectiveness is enhanced in the SOBP; eventually, the low impact of nuclear fragmentation makes helium ions suitable to treat cancers placed just before OARs. In order to obtain these data, $250-400$ MeV/u ^{4}He, ^{12}C and ^{16}O beams with C, C_2H_4 and PMMA targets will be used [34].

Thirdly, measurements performed with FOOT could be also interesting for other applications, such as radioprotection in space. NASA and other space agencies have started since several years the study of the risk assessment for astronauts in view of long duration space missions like a travel to Mars. Experimental data about nuclear interactions between different kinds of space radiation and human tissues are of paramount importance in order to study the most suitable spacecraft shielding. There are three main sources of energetic particles in space: Solar Particle Events (SPE), Galactic Cosmic Rays (GCR) and the geomagnetically trapped particles. SPE are mainly composed by protons emitted from the Sun during coronal mass ejections and solar flares: their energy spectrum can reach GeV region and, as SPE are unpredictable, they can inflict a lethal dose to the astronauts. GCR consist of high energy nuclei (from hydrogen to iron) produced by supernovae in the Milky Way galaxy: protons and alpha particles account for $\approx 98\%$ and the overall energy spectrum of radioprotection interest ranges from MeV to TeV. Even if heavy ions are very rare, they have an important effect on the total dose D, as $D \propto z^2$ and their damage on human tissues is poorly known up to now. The geomagnetically trapped particles consist of protons and electrons confined by the Earth magnetic field in two regions, called Van Allen belts. Trapped radiation originates from the interaction of GCR and solar particles with the Earth's magnetic field and the atmosphere. Electrons reach energies of up to 7 MeV and protons up to 600 MeV. A small fraction of heavier ions is also observed, at energies < 50 MeV/u. However, because of their limited penetration capacity, they are of no relevance for radiation protection [17]. The FOOT experiment will give precise cross section data in a poorly studied energy phase space of both SPE and GCR phenomena.

In the first section the inverse kinematics approach and the cross section subtraction method will be explained. In the second, the two detector setups will be presented. Eventually, expected performances will be summarized.

2.1 Inverse Kinematics and Cross Sections

Nuclear collisions in the Fermi energy range consist of bombarding a projectile on a fixed target nucleus. A part of the incident energy is spent as recoil energy of the centre of mass (CM), thus E_{CM} is only a fraction of the laboratory energy (E_{lab}) of the projectile; in a reference frame in which the target is at rest:

$$E_{\mathrm{CM}} = E_{\mathrm{lab}} \frac{A_t}{A_p + A_t}. \tag{2.1}$$

This expression is a non-relativistic approximation; E_{lab} is the beam energy, A_p and A_t the projectile and target mass number, respectively. The CM energy per nucleon writes as:

$$\epsilon_{\mathrm{CM}} = \frac{E_{\mathrm{CM}}}{A_p + A_t} = \frac{E_{\mathrm{lab}}}{A_p} \frac{A_p A_t}{(A_p + A_t)^2} = \epsilon_{\mathrm{lab}} \frac{A_p A_t}{(A_p + A_t)^2}. \tag{2.2}$$

The corresponding centre-of-mass velocity v_{CM} can be written as:

$$v_{\mathrm{CM}} = v_{\mathrm{lab}} \frac{A_p}{A_p + A_t}. \tag{2.3}$$

The expression *inverse kinematics* in nuclear physics is used when the projectile mass is larger than the target mass. From equation 2.2, the CM energy per nucleon has the same value for direct and inverse kinematics for a fixed incident energy per nucleon ϵ_{lab}. The inverse kinematics approach overcomes the difficulty to detect fragmentation products due to smashing protons which can travel only for a few tens of micrometres [21] and it allows to have a forward peaked distribution of heavy fragments within a polar angle of about 10° [35].

Thus, given a fragment produced by a proton projectile somewhere in the target material, the former can cross and leave the target only if it has been produced at a distance smaller than few micrometres from the exit surface of the target material. Otherwise the fragment deposits all its energy locally, being trapped inside the target, not allowing any possibilities of detection. Additionally, the energy lost by the fragments in the target is of the same order of magnitude of its initial energy, thus, unless it is possible to measure the initial positions with particularly high accuracy, the original kinetic energy of the fragments cannot be measured with adequate precision. Therefore a thick target must be excluded. On the other hand, also a very thin target can provide a great amount of issues: first of all it is technically difficult to create and handle item with such a small thickness ($\sim \mu$m). Moreover, the rate of fragmentation is extremely depressed, so it becomes excessively onerous to achieve a significant amount of data.

Therefore, the inverse kinematic approach in the FOOT experiment consists in changing roles of projectile and target: instead of protons, projectiles are nuclei (those part of the human body like ^{12}C, ^{16}O) and targets are protons, supposed at rest. By studying

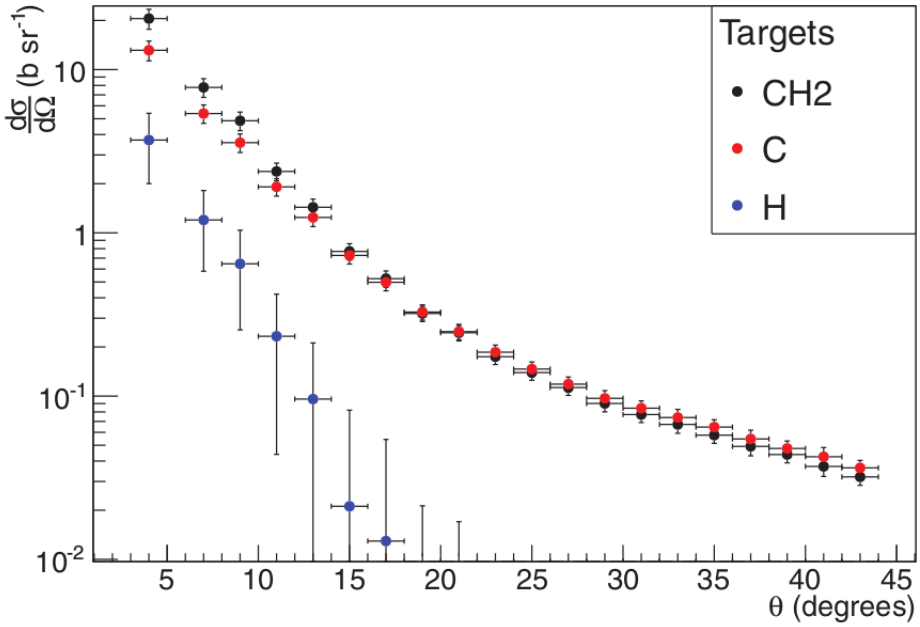

Figure 2.1: Combination of carbon and CH_2 targets angular distribution to determine the hydrogen angular distribution for α fragments. The angular distribution for the hydrogen target is the difference between both, divided by two [36].

the inverse interaction and measuring the four-momentum of the produced fragments, it is possible to gain experimental access to the direct decay chain information, performing a Lorentz transformation. In this way it is possible to take measurements with a thicker ($> \mu$m) target providing a higher fragmentation rate and significant amount of data, without the issues related to the direct kinematic approach.

This approach implies the management of a pure gaseous hydrogen target, which would lead to considerable technical difficulties in the clinical centres where the required beams are available. To avoid complications, it has been decided to adopt targets of polyethylene (C_2H_4) and graphite (C) and perform a subtraction of the measured cross sections:

$$\frac{d\sigma}{d\Omega}(H) = \frac{1}{4} \cdot \left(\frac{d\sigma}{d\Omega}(C_2H_4) - 2 \cdot \frac{d\sigma}{d\Omega}(C) \right). \tag{2.4}$$

The subtracting cross section method has already been used in [36] whose results are shown in figure 2.1.

Concerning the other FOOT goals, a direct kinematic approach can be used because fragments acquire enough energy to escape the target, allowing precise measurements of their momentum.

2.2 Experimental setup

In addition to inverse kinematic approach and radiobiological desiderata explained in the next section, the design of the FOOT experiment is driven by transport and space constraints: indeed, needed beams will be available in several treatment rooms and research centres requiring ease of moving. Moreover, the limited dimension of selected facilities, such as CNAO (*Centro Nazionale di Adroterapia Oncologica*) in Pavia (Italy) or HIT (*Heidelberg Ion Therapy*) centre in Heidelberg (Germany), constrains the detector length below $\sim$ 2 metres. A good balancing between the detector cost, its portability and the quest for the largest possible geometrical acceptance for the heavy forward peaked fragments can be found using a magnetic spectrometer composed by a permanent magnet with a high precision tracking system. However, the experience from previous experiments about nuclear fragmentation, together with the study of the relevant physics process by means of Montecarlo simulations, show that it is difficult to achieve the desired acceptance for light secondary fragments with an apparatus of limited size. The main reason comes from the fact that lower mass fragments, protons, deuterons and α particles can be emitted within a wider angular aperture with respect to heavier nuclei. Therefore, the necessary size and weight of a magnetic apparatus would become impracticable in view of a table top design. Therefore, the FOOT experiment will consist of two different setups [34]:

- a setup based on electronic detectors and a magnetic spectrometer concept, aiming at the identification and measurement of fragments heavier than ^{4}He, covering an angular acceptance up to 10 degrees from the beam axis;
- a setup exploiting a emulsion chamber detector. As already tested in the FIRST experiment [37], a specific emulsion chamber will be coupled with the interaction region of the FOOT setup to measure the production of light charged fragments such as protons, deuterons, tritons and α particles. The emulsion spectrometer supplies complementary measurements for large angle fragments with respect to the electronic detector, extending the angular acceptance up to about 70 degrees.

2.2.1 The Electronic Detector Setup

One of the main requirements of the FOOT detector design is a robust charge and isotopic identification of the produced fragments. Therefore the setup measures the following quantities of the produced fragments: momentum, kinetic energy, time of flight (TOF). The dE/dx of the fragment is measured twice through the energy release (ΔE) in a thin slab of plastic scintillator and in the silicon micro strip detector. The detector performances to be achieved are the following:

- momentum resolution $\sigma(p)/p$ at the level of 5%;

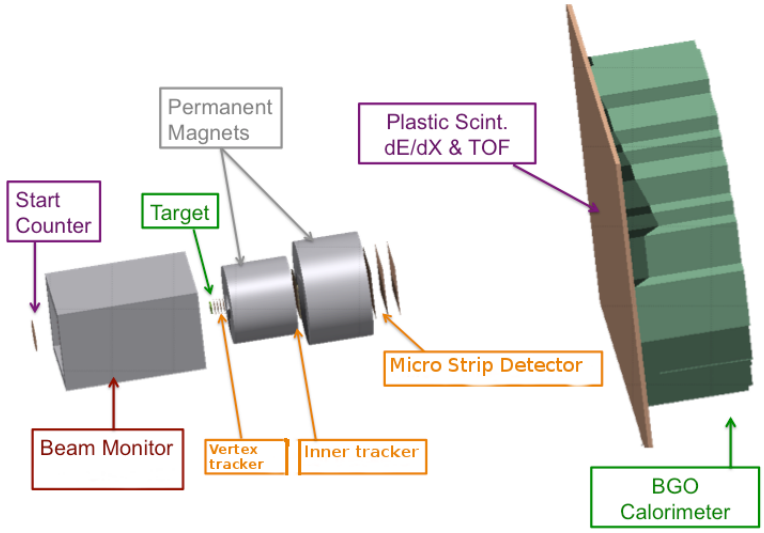

Figure 2.2: Schematic view of the FOOT apparatus.

- TOF resolution at the level of 100 ps;
- kinetic energy resolution $\sigma(E_k)/E_k$ at the level of 2%;
- energy release resolution $\sigma(\Delta E)/\Delta E$ at the level of 2%;
- energy differential cross section resolution ($d\sigma$ / dE) of the order of ~ 1 MeV/u.

The charge of the particle can be identified by combining ΔE measurements with TOF measurements, since $dE/dx \propto z^2 f(\beta)$.

The mass can be measured combining measurements of momentum, speed and energy through the following relations:

$$p = m\beta\gamma c, \tag{2.5}$$
$$E_k = mc^2(\gamma - 1), \tag{2.6}$$
$$E_k = \sqrt{p^2c^2 + m^2c^4} - mc^2, \tag{2.7}$$

where $\beta = v/c$ and γ is the Lorentz factor of the particle measured by the TOF detector.

The detector geometry is driven by two main factors: the emission angle of the (heavy) fragments and the angular separation between two fragments emitted in the same events; the former factor fixes the angular acceptance while the latter rules the granularity. The present setup in the downstream direction is presented in the following and it is shown in figure 2.2 [34]:

- Start Counter (SC): a 250 μm thick EJ-228 scintillator disk with a radius of 26 mm, read by fast PMT with 40% quantum efficiency and placed $20-30$ cm upstream of the target. It provides the trigger signal to the whole experiment, the start time for TOF measurement and the number of incoming ions to be used for cross sections normalization. A time resolution of the order of $\sigma_t = 100$ ps has been measured.

- Beam Monitor (BM): a drift chamber built for the FIRST experiment consisting of 12 layers of wires, with three drift cells per layer. Planes with wires along the x and y axes are alternated to reconstruct the beam profile. The cell shape is rectangular (16 mm×10 mm) with the long side orthogonal to the beam. In each view, two consecutive layers are staggered by half a cell to solve left-right ambiguities in track reconstruction. The BM was operated at atmospheric pressure, at the working voltage of 1.8 kV in Ar/CO2, 80/20 gas mixture. The BM efficiency was measured to be close to unity for carbon ion beam and the mean track spatial resolution was measured to be of the order of $\sim 140\,\mu$m. The BM detector will be placed between the SC and the target and will be used to measure the direction and impinging point of the ion beam on the target, a crucial information needed to address the pile-up ambiguity in the slow vertex (VTX) detector (readout time = 187 μs). In fact the BM read-out time, of the order of 1 μs or less, is fast enough to ensure that tracks belonging to different events will not be mixed.

- Target: polyethylene and graphite targets are needed to adopt the subtraction of cross section method explained above. The thickness of the target is chosen to be about 2 mm, avoiding both the fragment trapping effect and the excessive drop of the nuclear interaction rate.

- Vertex Tracker (VTX): it is composed of four identical sensors, each one consists of a matrix of 928×960 pixels of 20.7 μm pitch, for a size of the chip of 20.22 mm × 22.71 mm (figure 2.3). All four sensors are thinned to 50 μm. It provides the vertex position and it can be used also to reject events generated by fragmentations in the exit window of the BM.

- Permanent Magnet: two permanent magnets with Halbach geometry to supply the necessary curvature for the charged fragments in order to perform the momentum measurement. The Halbach cylindrical geometry provides a transverse magnetic field with a maximum of 0.8 T at the centre. With regard to material, two options are typically available, the SmCo (Samarium-Cobalt) and the NeFeB (Neodymium-Iron-Boron).

- Inner Tracker (IT): two planes of pixel sensors to measure both the position of the track in the plane orthogonal to the beam axis and the direction of the track itself. While the transverse displacements of the two sensing planes can be reconstructed from the data, their longitudinal distance requires a precise mechanics

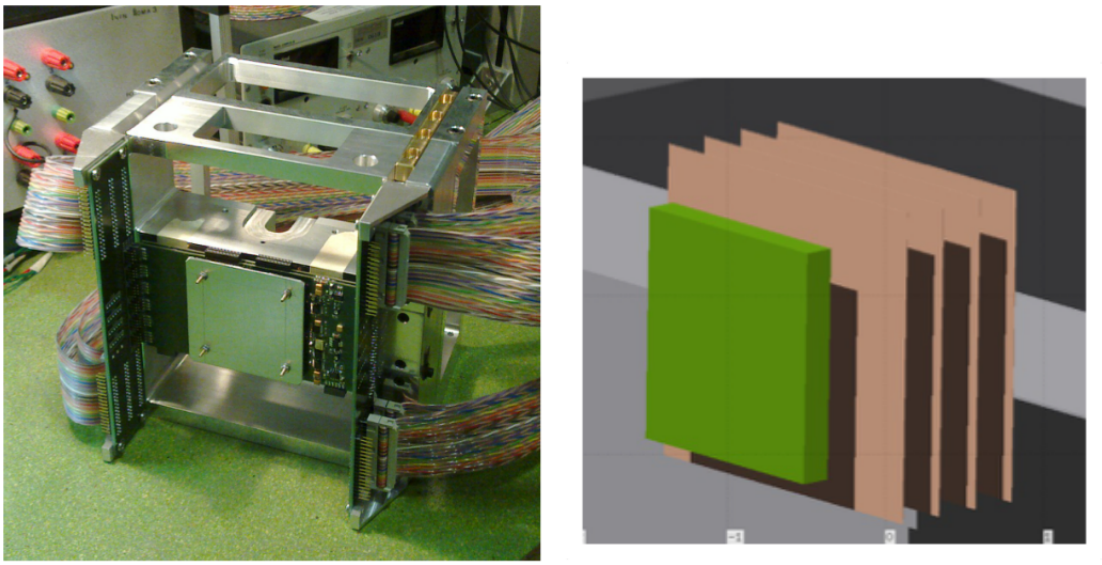

Figure 2.3: Target and vertex geometrical scheme.

with a spacer. Two planes of 16 sensors will be used, each sensor covering about $2 \times 2\,\mathrm{cm}^2$ for a overall area of $8 \times 8\,\mathrm{cm}^2$. The use of the same technology of VTX will simplify the DAQ, the procurement of the sensors and the need for specific know-how. The main rationale for these sensors thinned to $50\,\mu$m is the minimization of the multiple scattering and nucleus re-fragmentation like in the VTX.

- Microstrip Silicon Detector (MSD): it provides the tracking of fragments downstream the magnetic volume and the matching between the reconstructed tracks and the hits in TOF detector; it provides a dE/dx measurement for heavy ions up to $200 - 700\,\mathrm{MeV/u}$ kinetic energy range. The surface covered by MSD detector will be $9 \times 9\,\mathrm{cm}^2$; the three $x - y$ planes will be separated, one to each other, by a 2 cm gap along the beam direction, ensuring a compact measurement system. In order to reduce the amount of material needed for each measurement plane to $\sim 150\,\mu$m, and to ensure the $x - y$ coordinate readout, a solution exploiting two silicon planes thinned down to $70\,\mu$m each and glued together using a $30\,\mu$m thick bi-adhesive Kapton foil will be used, providing an equivalent silicon thickness of $\sim 155\,\mu$m.

- ΔE and TOF Detector: it provides the stop signal to the TOF measurement and the measurement of the energy release ΔE in a thin slab of plastic scintillator to identify the charge of the crossing fragment. This detector is made of two orthogonal layers of 20 plastic scintillator rods, each one 3 mm thick, 2 cm large and 40 cm long. The $40 \times 40\,\mathrm{cm}^2$ size matches the fragments aperture at 1 m distance

from the target. The 2 cm granularity matches the $2 \times 2\,\mathrm{cm}^2$ transverse surface of the calorimeter units and is enough to keep the occurrence of double fragments in the same rod below the % level. The dE/dx measurement should achieve accuracy of the order of $2 - 3\%$ while a 70 ps time resolution should be achieved on the heavy fragments (C,O) at 200 MeV/u, to fulfill the 100 ps requirement on TOF resolution.

- Calorimeter (CAL): it provides the energy of fragments produced in the target. The upper bound of the fragments energy range is defined by the beam energy, while the lower bound is set by the intensity of the magnetic field. FOOT will operate in a range where fragments are below the energy threshold that triggers a shower in a calorimeter. Therefore, the mechanisms for energy loss will be driven by the electromagnetic interaction and nuclear interactions: the production of neutrons escaping the calorimeter undetected produces a systematic underestimation of the initial energy. Since FOOT will work at a relatively low beam intensity, the ideal material for a calorimeter is a dense crystal, with high light yield, without strict requirements on the response speed. BGO is then a natural solution, also because it would open the opportunity to reuse crystals from past experiments. The typical transverse size of BGO crystals used for EM calorimeters corresponds approximately to the Molière radius, i.e. 2.2 cm. On the other hand, the thickness could vary, depending on the statistical and systematic requirements on the energy resolution.

2.2.2 The Emulsion Spectrometer

The experimental arrangement designed to detect the proton and the helium ion fragments is based on the *Emulsion Cloud Chamber* (ECC) concept. The start counter and the beam monitor are the same as the first experimental setup, as they provide information about the incident particle beam, while the other detectors are replaced by the ECC. The ECC consists in the integration of target and detector in a very compact setup: it is composed by a sequence of nuclear emulsion films (detector) interleaved with passive material of C and CH_2 (target). The passage of a charged particle in the nuclear emulsions produces a latent image which is turned into a sequence of silver grains after a complex chemical process known as *development*. All the grains are lied along the trajectory of the particle with a density almost proportional to the energy loss [38]. Through the nuclear emulsions it is possible to track the charged particle with a very high spatial resolution ($\sim 0.06\,\mu$m), providing an optimal angular resolution ($0.4 - 2$ mrad, depending on the scanning velocity) and it is also possible to retrieve the particle energy loss.

As shown in figure 2.4, the ECC structure for the FOOT experiment consists of three different sections: the first section acts as vertex tracker and it will be made of several

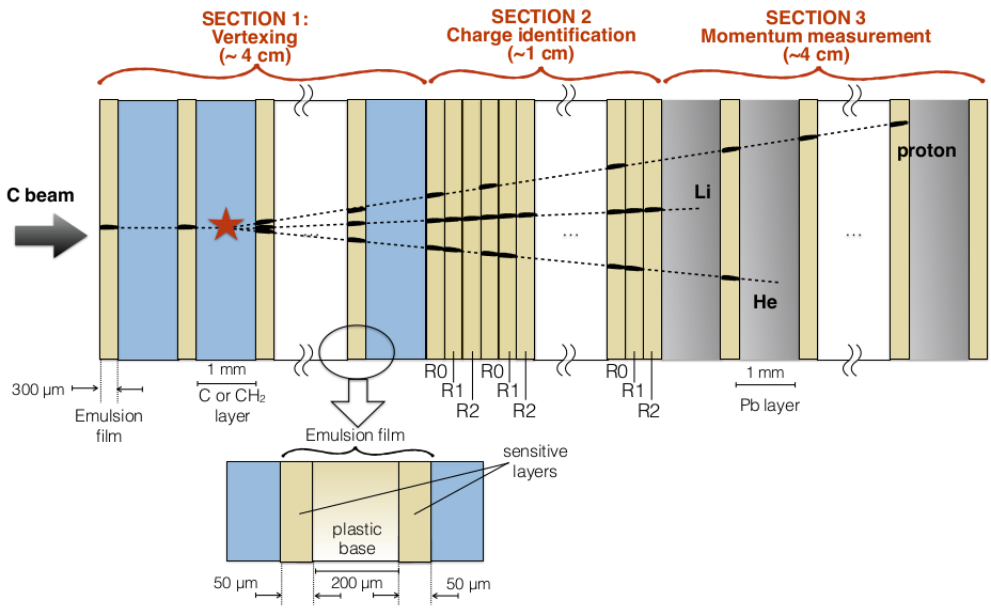

Figure 2.4: Scheme of ECC structure.

elementary cells made of Carbon or C_2H_4 layers (1 mm) alternated with emulsion films (300 μm). The ^{12}C ions will interact with the cells and originate secondary fragments. The detector emulsion structure will track the fragments and reconstruct the interaction vertex position with a micrometric resolution. The section 1 length will be optimized to achieve a statistically significant number of interactions.

The second section is dedicated to the charge identification for low Z fragments (mainly Hydrogen and Helium) and it will be composed by elementary cells, each containing three emulsion films only. As the specific ionization along the particle track is proportional to the grain density, the sum of the grain pixels belonging to the same track normalized to a given track length is a variable sensitive to the specific ionization, hence to the particle charge.

The third section, dedicated to momentum measurements, is made of emulsion films (300 μm thick) interleaved with 1 mm thick lead plates as passive material. The momentum will be evaluated with the range technique. Measuring the length of the whole particle track, its kinetic energy will be estimated on the basis of the correlation between range and momentum, using data supplied by NIST [12]. The section length will be set according to the incident beam energy; the number of lead plates will range between 10 and 50. The particle trajectory measurements, with high resolution in position and slope, provide also an estimate of the charged particle momentum through the MCS method (see equation 1.11): by using two independent methods for the energy and momentum estimate (i.e the range and multiple Coulomb scattering) the fragments mass for the

isotopic identification can be assessed.

2.3 Expected performances

The first goal for the cross section measurement of the produced fragments is their correct identification through the determination of its atomic (Z) and mass number (A). The performances have been obtained from simulated events with the electronic setup described in the previous section, analyzing 2.3×10^5 events (corresponding to 20 millions of incident particles) coming from the interaction of ^{16}O with 200 MeV/u on a C_2H_4 target. The Monte Carlo simulation is carried out by FLUKA code, which will be presented in the next chapter.

All the quantities necessary for the Z-A fragment identification derive from the time of flight (TOF), the momentum p, the energy release ΔE and the kinetic energy (E_k).

The TOF resolution has been obtained by the performance measured during a test beam; it has been parametrized as a function of Z and it corresponds to a percentage resolution in the range $1.8 - 2.4\%$. The velocity of the fragment is derived from TOF and the trajectory length of the track. The momentum reconstruction p has been determined by applying a gaussian smearing of 5% to the one generated independent on the momentum and types of fragments, as suggested by the results of track reconstruction presented in the next chapter. The energy release ΔE crossing a material has been reconstructed by the energy deposited in the plastic scintillator and its resolution has been parametrized as a function on the deposited energy and limited to the range $3 - 10\%$ as obtained at the test beam. The kinetic energy E_k has been reconstructed by adding the energy deposition in the plastic scintillator and in the calorimeter. The resolution on the deposited energy in the calorimeter has been obtained by a fixed gaussian smearing of 1.5% independent on the energy deposition. At the moment, it has been considered only the deposited energy of the primary fragment. The resolution on the Z-A identification is strongly dependent both on the energy loss by fragments due to ionization processes before reaching the calorimeter, and the leakage inside it mostly due to neutron emission.

Charge identification

The main detector dedicated to the Z determination is the plastic scintillator which provides the measurement of deposited energy and the TOF for the β determination. The Z determination is presented in figure 2.5 for all the studied fragments; every peak results well distinguished from each other, allowing a clear charge identification. The Z resolution improves with increasing fragment charge, from 6% for ^1H to 2% for ^{16}O. An improvement of the Z identification performances will be obtained combining the ΔE measurement of the plastic scintillator with the ΔE information from MSD.

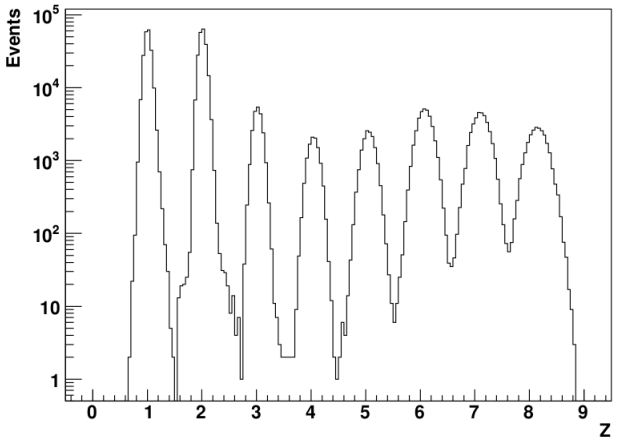

Figure 2.5: Determination of charge number Z for all the studied fragments.

Mass identification

The redundancy of subdetectors in FOOT is of paramount importance to improve mass identification. In particular, mass can be identified in three different ways:

- through β and p from TOF and the tracking system

$$A_1 = \frac{p}{u\beta c\gamma};$$

- through β and E_k from TOF and the calorimeter

$$A_2 = \frac{E_k}{uc^2(\gamma - 1)};$$

- through p and E_k from the tracking system and the calorimeter

$$A_3 = \frac{p^2c^2 - E_k^2}{2uc^2E_k}$$

where u is the unified atomic mass unit ($u \simeq 931.5\,\mathrm{MeV/c^2}$). The three different A determinations exhibit an obvious correlation because of the presence of a common subdetector for each couple of A definition.

To obtain these results, it is needed to reconstruct particle tracks in the magnetic spectrometer in order to find their momenta: for this reason, software plays a fundamental role both in simulation and in reconstruction processes. The details of the software of the FOOT experiment is presented in the next chapter.

Chapter 3

Software and track reconstruction

The simulation framework provides a tool to predict the detector performances in order to improve the experimental accuracy. It also helps to test the event reconstruction by combining the signals from different detectors. The reconstruction framework provides indeed several methods to study any target fragmentation event and it allows to calculate several useful quantities to pursue the FOOT goals. The software developed for the FOOT experiment is called SHOE (*Software for Hadrontherapy Optimization Experiment*) and it includes a general purpose toolkit for track reconstruction called GENFIT, based on the Kalman filter algorithm.

In the first and in the second section of this chapter, the simulation and the reconstruction framework will be discussed, respectively. In the third section the bases of Kalman filter algorithm will be described while in the fourth the GENFIT toolkit will be presented.

3.1 Simulation

The FOOT simulation has been built in the framework of the FLUKA code. FLUKA is a Monte Carlo (MC) code able to simulate transport and interaction of electromagnetic and hadronic particles in any target material over a wide energy range. It is a multi-purpose, multi-particle code that can be applied in many different fields [39]. In particular, many FLUKA developments, concerning both physics models and user interface, have been studied for its application in the context of hadrontherapy. For this purpose, FLUKA is used also at CNAO and HIT [40].

To run the simulation, the user must provide a description of the setup and some physical specifications, which have to be included in input geometry files. The required FLUKA input specifications are:

- dimensions and distances between the geometry regions, i.e. targets and detectors;

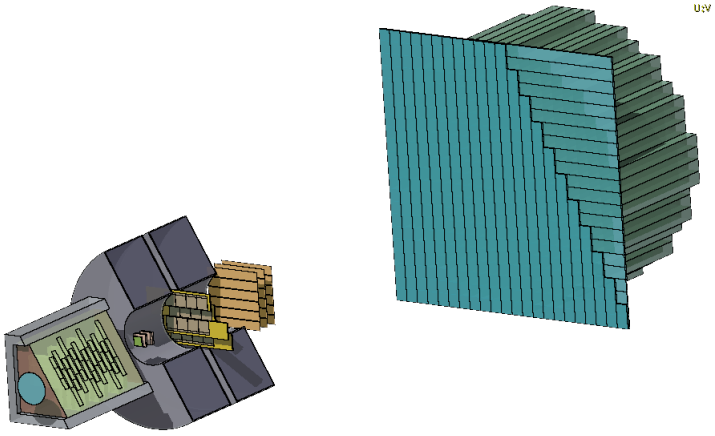

Figure 3.1: 3D rendering of the FOOT apparatus.

- material compositions and properties;
- source position, beam particle type, energy, spatial and/or momentum spread;
- magnetic field description;
- physics options (production and transport energy cut-off, δ rays production thresholds and activation of heavy fragments evaporation to achieve accurate results for residual nuclei production).

The entire setup geometry and materials have been accurately implemented in the input and geometry files. The MC code handles the transport of all primary and secondary particles throughout the experimental volume and scores the quantities of interest.

FLUKA has also an advanced user friendly interface called FLAIR which can be used to facilitate the editing of FLUKA input files, execution of the code and visualization of the output files [41]. A 3D rendering of the FOOT apparatus made by FLAIR is shown in figure 3.1. To simulate particles interactions with the various materials, FLUKA makes use of experimental cross sections, if available, otherwise different theoretical models are employed, according to the interacting particle type and energy as in the case of the FOOT experiment. Indeed, neither experimental data nor reliable model exist to describe nuclear interactions at these energies so FLUKA manages hadron-nucleus interaction with the PEANUT (Pre Equilibrium Approach to NUclear Thermalisation) model which is divided in intranuclear cascades, pre-equilibrium, evaporation and de-excitation steps.

On the other hand, nucleus-nucleus reaction models are mainly of two types. For initial ion energies up to 100 MeV/u the Boltzmann Master Equation (BME) approach is used, while at higher energies fragmentation processes are described by the relativistic Quantum Molecular Dynamics (rQDM) theory [42]. The BME model describes the

evolution of the de-excitation of the system of the two interacting nuclei during the pre-equilibrium phase. By solving a set of time-dependent transport equations, the model describes the evolution towards an equilibrium state through a sequence of two body reactions and ejection of unbound particles, whose multiplicity can be calculated. The rQDM model describes the interaction of two nuclei starting from their initial state described as a Fermi gas, following the propagation of each nucleon in the potential generated by all others nucleons and described according to a quantum mechanical formalism. The dynamical evolution of particles, the formation of heavy and light fragments and secondary nucleons is then predicted. All the models described until now, are coupled to the internal FLUKA models for the final relaxation step, which includes nuclear evaporation, fission, Fermi-breakup and gamma emission.

Regarding particle transport in the magnetic field, FLUKA approximates crossings between different regions by solving an equation (up to fourth grade) which combines the surface of the region and the particle helix trajectory in magnetic field. For the distance between two subsequent interaction a default accuracy of 0.05 cm is adopted in generic inputs. However, when dealing with very thin detectors of a few hundreds of μm or less as in the case of FOOT silicon detectors, an increased accuracy must be specified. The suitable accuracy value was set as the best compromise between the requested precision and the needed CPU time [34].

3.2 Reconstruction

In SHOE, the full reconstruction is performed by a ROOT based framework [43]. It uses hierarchical structure to obtain a solid and simple object-oriented architecture in which a final user customization level through several parameter files is guaranteed. While the I/O and the chain of algorithms are handled by the `TAGroot` and `TAGdata` base classes, the actual code executed for each event is provided by the user through the implementation of classes inheriting from `TAGaction`. Such algorithms need as input a ROOT ntuple (Monte Carlo data) and provide an output in the form of a `TAGdata` object that can be used by subsequent actions to perform structured tasks. Additionally, the actions can use `TAGpara` objects that are used to implement both the geometrical and calibration information of each detector and that can be retrieved and applied during the reconstruction process. The reconstruction software package handles the decoding of the data and simulation events, building in two main steps all the necessary input information to perform a full event reconstruction and analysis. The first step of the reconstruction code consists in reading, interpreting and converting in a single software-object format both the data and the simulation events provided in different input formats. In the second step, events are processed by track identification and reconstruction algorithm giving the needed information for the fragmentation studies and results. The basic diagram of SHOE code is sketched in figure 3.2. The first reconstruction level, called

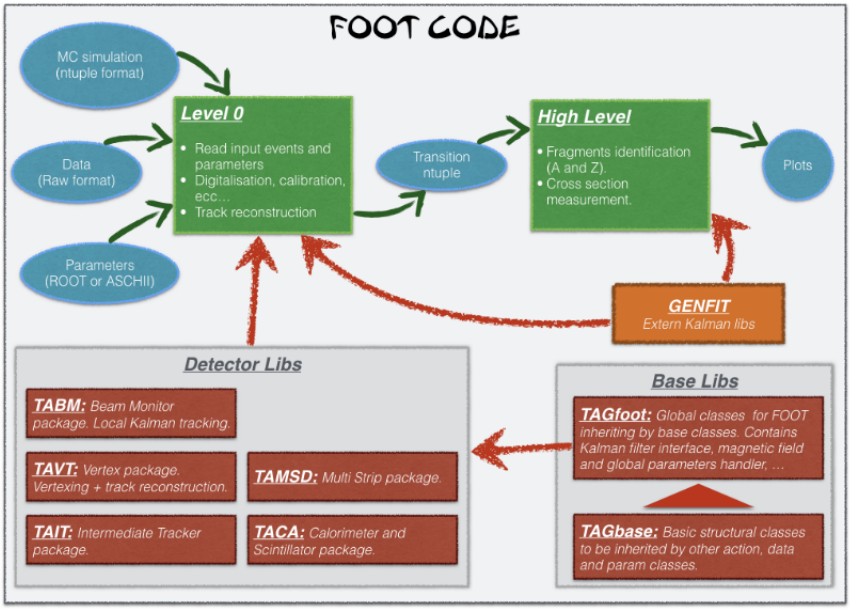

Figure 3.2: SHOE code diagram [34].

`Level0`, reads and decodes data from a ROOT ntuple and performs a track fitting using vertex detector, inner tracker and microstrip detector. The second reconstruction level, `HighLevel`, will also include the analysis code starting from fitted tracks.

A relevant fraction of time in the work for the present thesis has been dedicated to make uniformity in the FOOT geometry between the simulation and reconstruction frameworks. The details will be described in section 4.3.

3.3 Track fitting

The estimation of the kinematical parameters of a particle, as position, direction of flight and momentum along its trajectory is generally called as *track fitting*. Two standard track reconstruction methods will be described in the following. A very general approach to parameter estimation is the *Maximum Likelihood Method* (MLM): this method can take very general distributions of the observed variables into account, however, its application in multi-parameter problems can be very complex, in particular the error analysis. In cases where the distribution of the random variables is in first approximation Gaussian, at least approximately, the *Least Squares Method* (LSM) is generally successful [44].

Track fitting methods can be divided in *global* or *progressive* methods. In global methods, such as the LSM, the parameter estimation can be performed only when all

measurements are available: however, there are cases in which this requirement is not convenient, for example in real-time tracking of objects such as Intercontinental Ballistic Missile (ICBM) or in pattern recognition schemes which are based on track following, where it is not clear *a priori* if the hit combination under consideration does really belong to an actual track [44]. In these cases the use of progressive methods is preferred. Among them, the Kalman filter[a] is widely used for several purposes.

3.4 Least Squares Method

If the trajectory of a particle can be described by a closed form expression $f_{\boldsymbol{\lambda}}(\ell)$, where $\boldsymbol{\lambda}$ stands for the set of parameters, ℓ is the flight path and f is the coordinate which could be measured, a set of measurements m_i with errors σ_i will provide an estimate of the parameters according to the least squares principle:

$$\chi^2 = \sum_i \frac{(m_i - f_{\boldsymbol{\lambda}}(\ell_i))^2}{\sigma_i^2}. \tag{3.1}$$

The equation 3.1 must be minimized by setting its derivatives with respect to $\boldsymbol{\lambda}$ equal to zero, that is $\nabla\chi^2 = 0$. In the case of normally distributed measurements m_i, the LSM is equivalent to the MLM [45]. Symbolizing the derivative matrix of f with respect to the parameters as F and the (diagonal) error matrix of the measurements as $V = \operatorname{diag}\sigma_i^2$, the expression to be minimized is

$$\chi^2 = (\boldsymbol{m} - F\boldsymbol{\lambda})^T V^{-1} (\boldsymbol{m} - F\boldsymbol{\lambda}) \tag{3.2}$$

and requiring the derivative to vanish at the minimum leads to the matrix equation

$$F^T V^{-1} \boldsymbol{f} = F^T V^{-1} \boldsymbol{m}. \tag{3.3}$$

In case of a linear problem $\boldsymbol{f} = F\boldsymbol{\lambda}$, the above condition can be directly inverted

$$\boldsymbol{\lambda} = (F^T V^{-1} F)^{-1} F^T V^{-1} \boldsymbol{m} \tag{3.4}$$

and the estimated parameters are a linear function of the measurements [44].

The popularity of the LSM can be attributed to its optimality properties in the linear case: firstly, the estimate is *unbiased*, i.e. the expectation value of the estimate is the true value. Secondly, the estimate is *efficient*, which means that, among all unbiased estimates which are linear functions of the observables, the LSM estimate has the smallest variance (Gauss-Markov Theorem). Although these properties are strictly guaranteed only for the linear case, they are still retained in most cases where the function $f_{\boldsymbol{\lambda}}$ can be locally approximated by a linear expansion as in the FOOT experiment.

[a] Rudolf Emil Kálmán (1930 – −2016) was a Hungarian-born American electrical engineer, mathematician and inventor. He was most noted for his co-invention and development of the Kalman filter. For this work, U.S. President Barack Obama awarded Kálmán the National Medal of Science on October 7, 2009.

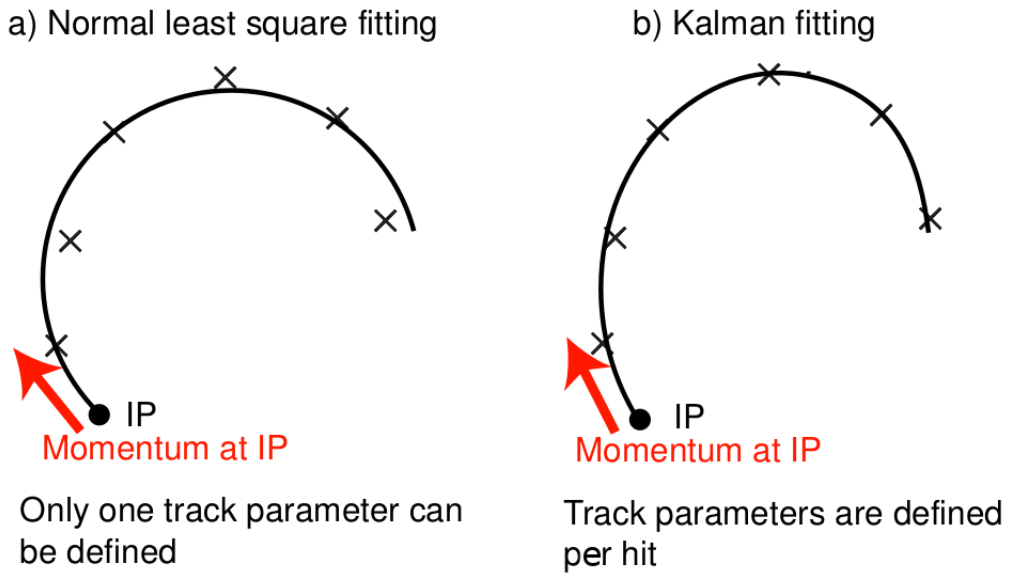

Figure 3.3: LSM fitting versus Kalman filter fitting [47].

3.5 The Kalman Filter technique

In discussing filtering and related problems, it is implicit that the systems under consideration are noisy. The noise may arise for a lot of reasons. For example, inputs to the system may be unknown and unpredictable except for their statistical properties, or outputs from the system may be derived with the aid of a noisy sensor [46]. The Kalman filter technique is an efficient recursive algorithm that finds the best estimate for the state of dynamic system from a set of noisy measurements [48, 49]. The filter is named after Rudolf E. Kálmán, one of the primary developers of this theory. Since it is a progressive method, it updates the knowledge about the trajectory with each new measurement so that no large matrices have to be inverted and the number of computations increases only linearly with the number of measurements in the track [50]: these features make the Kalman filter a very fast algorithm. Although the original Kalman filter is for a linear system, it can be extended to a non-linear one such as a charged particle trajectory in the FOOT magnetic field after a proper linearization of the system. In the following, the Extended Kalman Filter (EKF) will be presented even if it will be called simply Kalman filter.

3.5.1 State vector and measurement vector

In general a system is subject to random disturbance (*process noise*) during its evolution following an equation of motion (*system equation*). The goal of Kalman filter is to derive

the best estimate of the system state at a given point from information collected at multiple observation points (*measurement sites*). Assume that the state of the system can be specified by a p-dimensional column vector (*state vector*), $\bar{\boldsymbol{a}}_k$, where the suffix k denotes the site at which the state is given and the bar over a indicates the true value. The system equation that describes the evolution of the state $\bar{\boldsymbol{a}}_{k-1}$ at site $(k-1)$ to $\bar{\boldsymbol{a}}_k$ at site (k) can be written as [47]:

$$\bar{\boldsymbol{a}}_k = \boldsymbol{f}_{k-1}(\bar{\boldsymbol{a}}_{k-1}) + \boldsymbol{w}_{k-1} \tag{3.5}$$

where $\boldsymbol{f}_{k-1}(\bar{\boldsymbol{a}}_{k-1})$, which is a non-linear function in general, is a *state propagator* corresponding to a smooth deterministic motion expected if the random disturbances due to the process noise, $\boldsymbol{w}_{k-1}$, were absent. For the sake of argument, the process noise is unbiased, $\langle \boldsymbol{w}_{k-1} \rangle = 0$ and it has a covariance given by

$$\boldsymbol{Q}_{k-1} \equiv \langle \boldsymbol{w}_{k-1} \boldsymbol{w}_{k-1}^T \rangle. \tag{3.6}$$

At each measurement site, detectors measure one or more observables. The values of these observables at site (k) forms an m-dimensional column vector called *measurement vector*, $\boldsymbol{m}_k$. The relation between the measurement vector and the state vector is a *measurement equation*:

$$\boldsymbol{m}_k = \boldsymbol{h}_k(\bar{\boldsymbol{a}}_k) + \varepsilon_k, \tag{3.7}$$

where $\boldsymbol{h}_k(\bar{\boldsymbol{a}}_k)$ gives the resulting measurement vector if the random errors due to the *measurememt noise* ε_k are absent. For assumption, measurement noise is unbiased, $\langle \varepsilon_k \rangle = 0$ i.e. detectors are perfectly aligned, and its covariance is given by

$$\boldsymbol{V}_k \equiv (\boldsymbol{G})^{-1} \equiv \langle \varepsilon_k \varepsilon_k^T \rangle. \tag{3.8}$$

In the reconstruction framework of the FOOT experiment, the state vector is a 5D vector which contains a track parametrization in plane coordinates, i.e. $\bar{\boldsymbol{a}}_k = \begin{pmatrix} q/p & u' & v' & u & v \end{pmatrix}^T$ where q/p is particle charge over momentum, u' and v' are direction tangents, u and v are positions on the detector. The measurement vector depends on detector type but generally it is a 3D vector which contains hit coordinates. The process noise is due to Multiple Coulomb Scattering and energy-loss straggling while the measurement noise is random detector noise.

3.5.2 Prediction

In the *prediction* step, the state vector at site (k) from the measurements made at sites up to $(k-1)$ is predicted. It is indicated as $\boldsymbol{a}_k^{k-1}$. As process noise is at present unknown, in the equation 3.5 only the state propagator is considered, so that

$$\boldsymbol{a}_k^{k-1} = \boldsymbol{f}_{k-1}(\boldsymbol{a}_{k-1}^{k-1}) = \boldsymbol{f}_{k-1}(\boldsymbol{a}_{k-1}). \tag{3.9}$$

By definition, the covariance matrix (error matrix) for $\boldsymbol{a}_{k-1}$ is given by:

$$\boldsymbol{C}_{k-1} \equiv \langle (\boldsymbol{a}_{k-1} - \bar{\boldsymbol{a}}_{k-1})(\boldsymbol{a}_{k-1} - \bar{\boldsymbol{a}}_{k-1})^T \rangle. \tag{3.10}$$

Similarly, the covariance matrix for the predicted state vector $\boldsymbol{a}_k^{k-1}$ expressed in terms of $\boldsymbol{C}_{k-1}$ is given by:

$$\boldsymbol{C}_k^{k-1} \equiv \langle (\boldsymbol{a}_k^{k-1} - \bar{\boldsymbol{a}}_k)(\boldsymbol{a}_k^{k-1} - \bar{\boldsymbol{a}}_k)^T \rangle = \boldsymbol{F}_{k-1} \boldsymbol{C}_{k-1} \boldsymbol{F}_{k-1}^T + \boldsymbol{Q}_{k-1}, \tag{3.11}$$

where

$$\boldsymbol{F}_{k-1} \equiv \left(\frac{\partial \boldsymbol{f}_{k-1}}{\partial \boldsymbol{a}_{k-1}} \right) \tag{3.12}$$

is called *propagator matrix* [47].

3.5.3 Filtering

In the *filtering* step, the predicted state vector $\boldsymbol{a}_k^{k-1}$ is updated by including information acquired at site (k). As for the previous step, it is important to keep a recursive algorithm. All available information about the state vector at site (k) from measurements up to site $(k-1)$ can be summarized in a single χ^2:

$$(\chi^2)_k^{k-1} = (\chi^2)_{k-1} + (\boldsymbol{a}_k^\star - \boldsymbol{a}_k^{k-1})^T (\boldsymbol{C}_k^{k-1})^{-1} (\boldsymbol{a}_k^\star - \boldsymbol{a}_k^{k-1}) \tag{3.13}$$

where $\boldsymbol{a}_k^\star$ is a new estimate of the state vector at site (k) to be updated with the information collected at the site (k) and $(\chi^2)_{k-1}$ is the χ^2 up to the site $(k-1)$ and it is independent of $\boldsymbol{a}_k^\star$. Furthermore, it is possible to add information about the new measurement performed at the site (k):

$$(\chi^2)_k^k = (\boldsymbol{m}_k - \boldsymbol{h}_k(\boldsymbol{a}_k^\star))^T \boldsymbol{G} (\boldsymbol{m}_k - \boldsymbol{h}_k(\boldsymbol{a}_k^\star)). \tag{3.14}$$

Assuming that $\boldsymbol{a}_k^\star - \boldsymbol{a}_k^{k-1}$ is small it is possible to keep the first order term in Taylor expansion only:

$$\boldsymbol{h}_k(\boldsymbol{a}_k^\star) \simeq \boldsymbol{h}_k(\boldsymbol{a}_k^{k-1}) + \boldsymbol{H}_k(\boldsymbol{a}_k^\star - \boldsymbol{a}_k^{k-1}), \tag{3.15}$$

where

$$\boldsymbol{H}_k \equiv \left(\frac{\partial \boldsymbol{h}_k}{\partial \boldsymbol{a}_k^{k-1}} \right) \tag{3.16}$$

is called *projector matrix*. As $(\chi^2)_{k-1}$ does not depend on $\boldsymbol{a}_k^\star$, the quantity to minimize is

$$\chi_+^2 = (\boldsymbol{a}_k^\star - \boldsymbol{a}_k^{k-1})^T (\boldsymbol{C}_k^{k-1})^{-1} (\boldsymbol{a}_k^\star - \boldsymbol{a}_k^{k-1}) + (\boldsymbol{m}_k - \boldsymbol{h}_k(\boldsymbol{a}_k^\star))^T \boldsymbol{G}_k (\boldsymbol{m}_k - \boldsymbol{h}_k(\boldsymbol{a}_k^\star)). \tag{3.17}$$

By minimizing χ_+^2 with respect to $\boldsymbol{a}_k^\star$ one obtains the update of the state vector:

$$\boldsymbol{a}_k = \boldsymbol{a}_k^{k-1} + \boldsymbol{K}_k(\boldsymbol{m}_k - \boldsymbol{h}_k(\boldsymbol{a}_k^{k-1})), \tag{3.18}$$

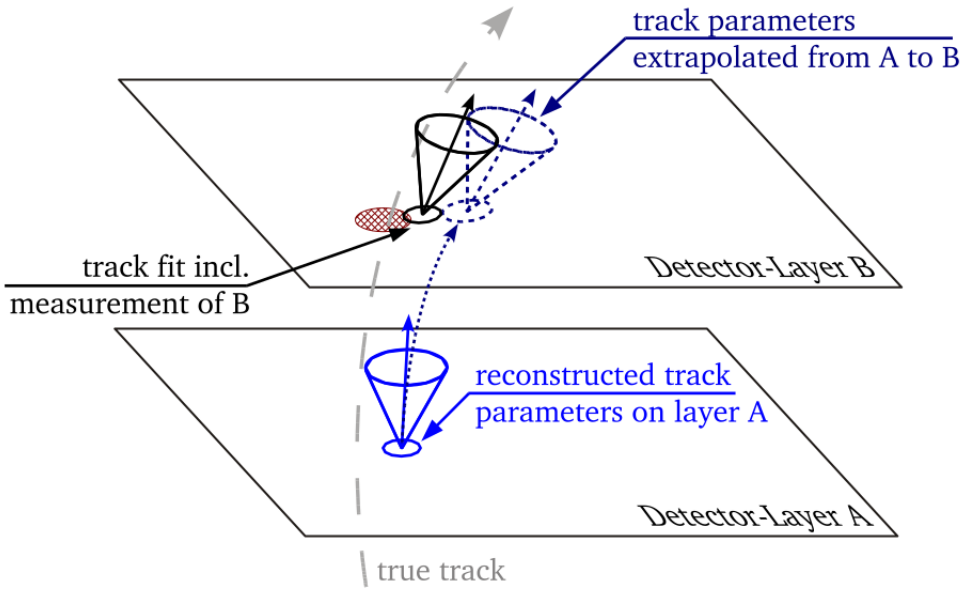

Figure 3.4: Functional principle of the Kalman filter. The reconstructed track parameters on surface A are extrapolated to surface B. On surface B, using the measurememt, an update is performed. [51].

where

$$\boldsymbol{K}_k = \boldsymbol{C}_k^{k-1}\boldsymbol{H}_k^T\left(\boldsymbol{V}_k + \boldsymbol{H}_k\boldsymbol{C}_k^{k-1}\boldsymbol{H}_k^T\right)^{-1} = \boldsymbol{C}_k\boldsymbol{H}_k^T\boldsymbol{G}_k. \tag{3.19}$$

The matrix $\boldsymbol{K}_k$ is called *Kalman Gain Matrix* and it represents how much the new measurement at site (k) improves the predicted state vector. Thanks to the Kalman Gain Matrix one can finally calculate the new covariance matrix $\boldsymbol{C}_k$, the residual $\boldsymbol{r}_k$, the covariance matrix of the residual $\boldsymbol{R}_k$ and the χ^2 increment χ^2_+ [50]:

$$\boldsymbol{C}_k = (\mathbb{1} - \boldsymbol{K}_k\boldsymbol{H}_k)\boldsymbol{C}_k^{k-1} \tag{3.20}$$

$$\boldsymbol{r}_k = \boldsymbol{m}_k - \boldsymbol{H}_k\boldsymbol{a}_k = (\mathbb{1} - \boldsymbol{H}_k\boldsymbol{K}_k)\boldsymbol{r}_k^{k-1} \tag{3.21}$$

$$\boldsymbol{R}_k = (\mathbb{1} - \boldsymbol{H}_k\boldsymbol{K}_k)\boldsymbol{V}_k \tag{3.22}$$

$$\chi^2_+ = r_k^T\boldsymbol{R}_k^{-1}r_k. \tag{3.23}$$

3.5.4 Smoothing

In general, the state vector obtained at site (k) in the filtering process is the optimal at that point with the information of all the states up to $(k-1)$. The state vector at site (k) can, however, be re-evaluated and further improved after accumulating more information

at subsequent sites, from $(k+1)$ to (n). This process is called *smoothing* [47]. Thus, smoothing is a recursive operation which proceeds step by step in the direction opposite to that of the filtering. The quantities used in each step have been calculated in the preceding filtering process. If process noise (e.g. the Multiple Coulomb Scattering) is taken into account, the smoothed trajectory may in general contain small kinks and thus reproduce more closely the real path of the particle [44]. The smoothed state vector at site (k) containing information from $(k+1)$ to (n) is given by:

$$\boldsymbol{a}_k^n = \boldsymbol{a}_k + \boldsymbol{A}_k(\boldsymbol{a}_{k+1}^n - \boldsymbol{a}_{k+1}^k) \tag{3.24}$$

where

$$\boldsymbol{A}_k = \boldsymbol{C}_k \boldsymbol{F}_k^T (\boldsymbol{C}_{k+1}^k)^{-1}. \tag{3.25}$$

For further details about the smoothing step see [47].

3.6 The Deterministic Annealing Filter

The obvious way of protecting against wrong hits is a selection procedure based on the residuals. The problem of insufficient information in the initial phase of the filter can be overcome by adopting an iterative procedure. After a first round of filter plus smoother the track position can be predicted in every layer, using information from all the other layers. Based on these predictions, the assignment probabilities of all competing hits can be computed in every layer. If this probability falls below a certain threshold, the hit is suppressed during the next iteration. It is, however, not excluded that the hit is used again in a later iteration. The assignment probabilities of the remaining hits are normalized to one and used as the weights in the next iteration of the filter. If all hits are eliminated the sum of the assignment probabilities is equal to zero and no normalization is possible. This requires some modification to the filter update formulas, effectively allowing the weights to sum to any number in the interval $[0, 1]$.

The filter itself is a Kalman filter with reweighted observations [52] as it can be seen in figure 3.5. The propagation part is identical to the standard case and the prescription for the update of the state vector at step (k) is a Kalman filter with prediction $\boldsymbol{a}_k^{k-1}$ and a set of measurement $\boldsymbol{m}_k^i$. If p_k^i is the assignment probability of observation $\boldsymbol{m}_k^i$, its weight matrix is $p_k^i \boldsymbol{V}_k^{-1}$. This leads to the following update of the state vector:

$$\boldsymbol{a}_k = \boldsymbol{a}_k^{k-1} + \boldsymbol{K}_k \sum_{i=1}^{n_k} p_k^i (\boldsymbol{m}_k^i - \boldsymbol{H}_k \boldsymbol{a}_k^{k-1}) \tag{3.26}$$

where n_k is the number of competing hits at the site (k). $\boldsymbol{K}_k$ has to be written in terms of the inverse covariance or weight matrices to allow for zero weights

$$\boldsymbol{K}_k = ((\boldsymbol{C}_k^{k-1})^{-1} + p_k \boldsymbol{H}_k^T \boldsymbol{V}_k^{-1} \boldsymbol{H}_k)^{-1} \boldsymbol{H}_k^T \boldsymbol{V}_k^{-1}, \tag{3.27}$$

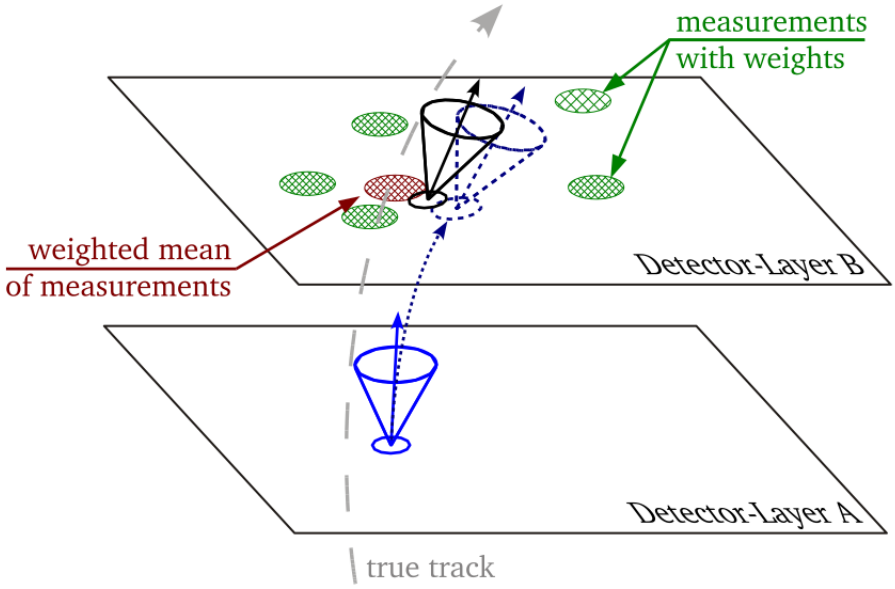

Figure 3.5: The DAF uses the same principle as the Kalman filter, but several measurements per detector layer are taken into account by using their weighted mean [51].

where p_k is the sum over all weights p_k^i. As in the standard Kalman filter, the covariance matrix $\boldsymbol{C}_k$ of the updated $\boldsymbol{a}_k$ is given by the first factor of the gain matrix [52]:

$$\boldsymbol{C}_k = ((\boldsymbol{C}_k^{k-1})^{-1} + p_k \boldsymbol{H}_k^T \boldsymbol{V}_k^{-1} \boldsymbol{H}_k)^{-1}. \tag{3.28}$$

The assignment weights are proportional to the Gaussian probability density function, using the measurement $\boldsymbol{m}_k^i$ and the smoothed state $\boldsymbol{a}_k^n$ on a particular surface:

$$\phi_i = \frac{1}{(2\pi)^{n/2}\sqrt{\det \boldsymbol{V}_k}} \exp\left[\frac{1}{2}(\boldsymbol{m}_i - \boldsymbol{H}_k \boldsymbol{a}_k^n)\boldsymbol{V}_k^{-1}(\boldsymbol{m}_i - \boldsymbol{H}_k \boldsymbol{a}_k^n)^T\right]. \tag{3.29}$$

Finally, the assignment weights are normalized:

$$p_k^i = \frac{\phi_i}{\sum_{j=1}^n \phi_j + \sum_{j=1}^n \phi_{\mathrm{j,cut}}} \tag{3.30}$$

where $\phi_{\mathrm{j,cut}}$ is a cut-off value which forces the assignment probability to be close to zero if the probability of a hit falls below a certain value. For example, if a 2-dimensional hit with a probability lower than 0.001 should be suppressed, $\phi_{\mathrm{j,cut}}$ is [53]:

$$\phi_{\mathrm{j,cut}} = \frac{1}{(2\pi)\sqrt{\det \boldsymbol{V}_k}} \exp\left[\frac{1}{2}\frac{13.81551}{T}\right]. \tag{3.31}$$

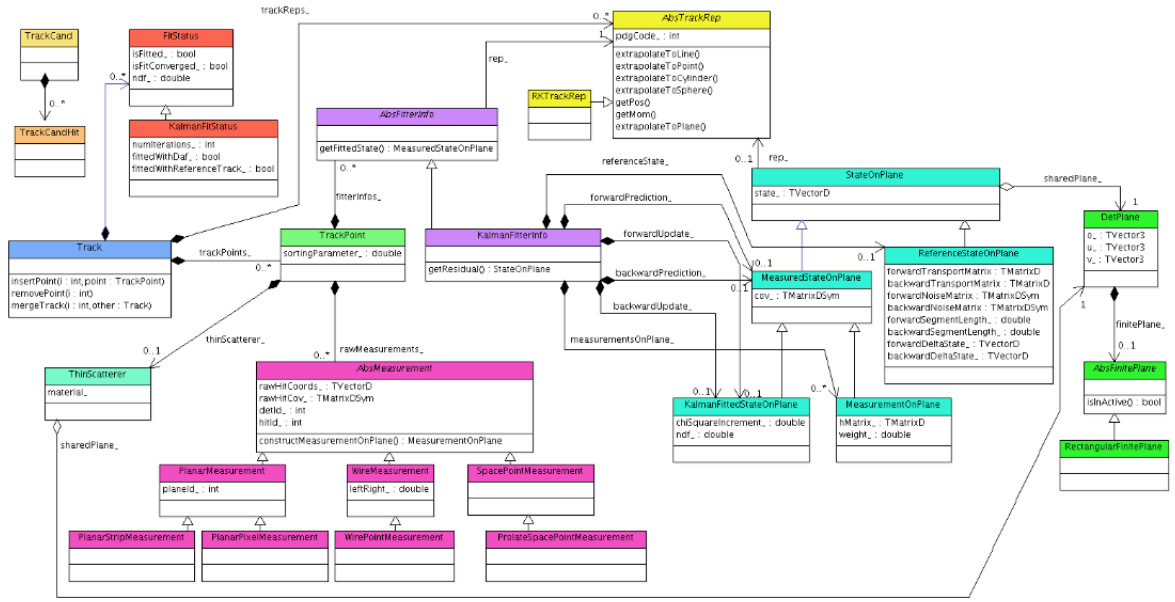

Figure 3.6: GENFIT class diagram [54].

The *temperature* parameter $T = 1/\beta$ (dimensionless with $0 < \beta \leq 1$) is introduced by the DAF to avoid local optima. This factor blows up the covariances of the competing measurements which means that even measurements being farther away from the initial track estimate are taken into account at high temperature [51].

3.7 GENFIT

The Kalman filter implementation in the FOOT experiment is based on the experiment-independent open source GENFIT library [54]. GENFIT provides an extensible modular open-source framework that performs track fitting and other related tasks and thus eliminates the redundancy of writing track-fitting programs for every experiment. GENFIT was successfully used during a test of the Belle II high-level trigger architecture and the combined Belle II vertex-detector readout architecture. There it served for online track reconstruction in the data-reduction stage of the high-level trigger, as well as for offline analysis. Track fitting in GENFIT is based on three pillars: *measurements*, *track representations*, and *fitting algorithms*. The block diagram of GENFIT library is reported in figure 3.6. Measurements serve as objects containing measured coordinates from a detector. They provide functions to construct a (virtual) detector plane and to provide measurement coordinates and covariance in that plane. The abstract base class `AbsMeasurement` defines the interface. GENFIT comes with predefined measurement classes for various detector types, including planar detectors, drift chambers, and time

projection chambers.

Track representations combine track-parameterization and track-extrapolation code. GENFIT implements a track representation (`RKTrackRep`) based on a Runge-Kutta extrapolator from GEANT3. An abstract interface class interacts with the detector geometry and implementations using ROOT `TGeoManager` are available. During fitting, material properties are used to calculate the following effects: energy loss and energy-loss straggling for charged particles according to the Bethe-Bloch formula; multiple scattering, where the full noise matrix is calculated; soft Bremsstrahlung energy loss and energy-loss straggling for e^- and e^+. The step size used for the Runge-Kutta extrapolation should be as large as possible to save unnecessary computation while still being small enough to keep errors reasonably small. An adaptive step-size calculation is done in the `RKTrackRep` taking field inhomogeneities and curvature into account.

Eventually, fitting algorithms use measurements and track representations to calculate fit results exploiting a `Track` object. This object contain a lot of information such as measurements and one or more track representations belonging to different particle hypotheses that should be fitted. Moreover, it contains a `FitStatus` object, which stores general information (number of iterations, convergence) and fit properties (χ^2, degrees of freedom, p-value, track length) [54]. As convergence criteria, a minimum and maximum number of iterations can be set, which are 2 and 4 by default. After the minimum number of iterations, GENFIT checks if the p-value has changed less than a certain amount since the previous iteration; the default is 10^{-3}. However, tracks with a p-value close to zero are often considered as converged with this criterion, even though the χ^2 is still changing significantly, indicating that the fit is still improving. This occurs often for tracks that received very wrong start parameters. To cure this issue, a nonconvergence criterion has been introduced: if the relative change in χ^2 from one iteration to the next is larger than 20%, the fit will continue. This number is user-adjustable, too.

GENFIT provides four different fitters: the standard Kalman filter, the Kalman filter with a reference track (it is convenient when state predictions fall very far from real trajectories), the Deterministic Annealing Filter and the General Broken Lines (GBL) fitter (it is mathematically equivalent to the Kalman fitter with thin scatterers instead of continuous materials but it fits tracks entirely in one step) [54].

Chapter 4

Interface to the FOOT geometry

The first goal of this master thesis was to make uniformity in the geometry between the reconstruction code and the FLUKA simulation. This goal is of primary importance in particular in the current optimization phase of the experiment, where many changes in the geometrical setup can still take place. In the first section of this chapter, FLUKA handling of the FOOT geometry will be summarized. In the second, SHOE classes for geometry of the experiment will be discussed. In the last, the software updates apported by myself will be presented.

4.1 Geometry in FLUKA

FLUKA handles the geometry relying on the principle of combinatorial geometry: several basic convex shapes, called *bodies*, such as cylinders, spheres, parallelepipeds are combined with each other to create more complex shapes called *regions*. This combination is performed using boolean operations such as union, intersection and subtraction. The input for each body consists of:

- the code indicating the body type (RPP stands for rectangular parallelepiped, XYP for a plane perpendicular to z-axis, RCC for right circular cylinder);
- a unique body name assigned by the user;
- a set of geometrical quantities defining the body, different for each body type (e.g. RPP requires $x_{\min}$, $x_{\max}$, $y_{\min}$, $y_{\max}$, $z_{\min}$, $z_{\max}$).

Regions are not necessarily simply connected (they can be made as the union of two or more non contiguous or partially overlapping zones) but they must be made of homogeneous material. A region definition requires a name and a sequence of one or more body names, preceded by the operators + (intersection) or − (complement or substraction).

In order to avoid infinite tracking, the user has to define a region outside the detector assigning the material `BLCKHOLE` to it.

There are more than 80 option keywords available for input in FLUKA and some of them are contained in `foot.inp` file. For instance, the keyword `ASSIGNMA` defines the correspondence between region and material indices and defines regions where a magnetic field exists; `BEAM` defines most of the beam characteristics (energy, profile, divergence, particle type); `BEAMPOS` defines the starting point of beam particles and the beam direction; `MATERIAL` and `COMPOUND` which define a material and a mixture or compound, respectively. In `foot.geo` file, both bodies and regions of the FOOT experiment are defined as in the example below.

```
* ***Inner Tracker
RPP itrbox    -3.000000 3.000000 -3.000000 3.000000 13.882000 14.118000
XYP itr00     13.887000
XYP itr01     13.888000
XYP itr02     13.890500
XYP itr03     13.891500
XYP itr04     13.896500
XYP itr05     13.897500
XYP itr06     13.900000
XYP itr07     14.100000
XYP itr08     14.102500
XYP itr09     14.103500
XYP itr10     14.108500
XYP itr11     14.109500
XYP itr12     14.112000
XYP itr13     14.113000

* ***Inner Tracker
ITR0          5 itrbox +itr00
ITR1          5 itrbox -itr13
ITREPO0       5 itrbox -itr00 +itr01
ITREPO1       5 itrbox -itr12 +itr13
ITRAL0        5 itrbox -itr02 +itr03
ITRAL1        5 itrbox -itr04 +itr05
ITRAL2        5 itrbox -itr08 +itr09
ITRAL3        5 itrbox -itr10 +itr11
ITRCOV0       5 itrbox -itr01 +itr02
ITRCOV1       5 itrbox -itr05 +itr06
ITRCOV2       5 itrbox -itr07 +itr08
ITRCOV3       5 itrbox -itr11 +itr12
ITRKAP0       5 itrbox -itr03 +itr04
ITRKAP1       5 itrbox -itr09 +itr10
ITRFOAM       5 itrbox -itr06 +itr07
```

In this code, a single parallelepiped body `itrbox` for the inner tracker detector is defined and then sliced with planes perpendicular to z-axis. In order to ensure the best compatibility between simulation and reconstruction framework, as in ROOT it is not possible

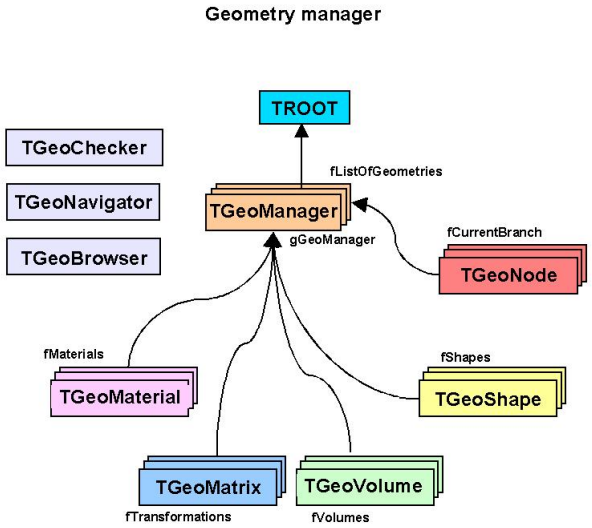

Figure 4.1: Geometry class diagram [43].

to define bodies in such a way, we decided to modify the previous code and to define parallelepipeds one by one. Then, regions are created combining bodies using boolean operations. If a body name is preceded by a + operator in an expression describing a region, it means that the region is fully contained inside the body (boolean intersection). If a body name is preceded by a − operator, it means that the region is fully outside the body (boolean complement).

4.2 Geometry in SHOE

The ROOT geometry package is a CERN tool used also for building, browsing, navigating and visualizing detector geometries [55]. The code works standalone with respect to any tracking Monte Carlo engine; therefore, it does not contain any constraints related to physics. However, the navigation features provided by the package are designed to optimize particle transport through complex geometries, working in correlation with simulation packages such as GEANT3, GEANT4 and FLUKA [43]. In order to simplify the creation of material and mixture, one can use the pre-built table of elements owned by `TGeoManager` class.

The basic bricks for building up a geometrical model are called *volumes*. These represent the unpositioned pieces of the geometry puzzle. The relationship between the pieces is not defined by neighbors, but by containment: volumes are inserted one inside

another making an in-depth hierarchy. These volumes for every detector are defined in `parGeo` classes, one for each detector. In the code shown below you can see an example from `TAITparGeo` class for inner tracker detector, where several `TGeoVolume` box-shaped objects are created.

```
TGeoVolume *box = gGeoManager->MakeBox("ITbox",
gGeoManager->GetMedium("AIR"),
width_Lx/2,height_Ly/2,m_dimension.z()/2);
gGeoManager->SetTopVisible(1);

TGeoVolume *siliconFoil = gGeoManager->MakeBox("siliconFoil",
gGeoManager->GetMedium("SILICON"),width_Lx/2,height_Ly/2,
m_siliconSensorThick_Lz/2);

TGeoVolume *kaptonFoil = gGeoManager->MakeBox("kaptonFoil",
gGeoManager->GetMedium("KAPTON"),
width_Lx/2,height_Ly/2,
m_materialThick[ "ITR_KAP_MEDIUM" ]/2);

TGeoVolume *coverKaptonFoil = gGeoManager->MakeBox("coverKaptonFoil",
gGeoManager->GetMedium("KAPTON"),width_Lx/2,height_Ly/2,
m_materialThick[ "ITR_COV_MEDIUM" ]/2);
```

When creating a volume one does not specify if this will contain or not other volumes. Adding daughters to a volume implies creating those and adding them one by one to the list of daughters. Since the volume has to know the position of all its daughters, we will have to supply at the same time a geometrical transformation with respect to its local reference frame for each of them. The objects referencing a volume and a transformation are called *nodes* and their creation is fully handled by the modeler. They represent the link elements in the hierarchy of volumes. Nodes are unique and distinct geometrical objects only from their container point of view. Since volumes can be replicated in the geometry, the same node may be found on different branches. In the same code, volumes are put side by side.

```
box->AddNode(siliconFoil, c++ , new TGeoCombiTrans(0,0,
position+=( m_materialThick[ "ITR_MEDIUM" ]/2 ),
new TGeoRotation("null,",0,0,0)));
box->AddNode(epoxyFoil, c++ , new TGeoCombiTrans(0,0,
position+=( m_materialThick[ "ITR_MEDIUM" ]/2
+ m_materialThick[ "ITR_EPO_MEDIUM" ]/2 ),
new TGeoRotation("null,",0,0,0)));
box->AddNode(coverKaptonFoil, c++ , new TGeoCombiTrans(0,0,
position+=( m_materialThick[ "ITR_EPO_MEDIUM" ]/2 +
m_materialThick[ "ITR_COV_MEDIUM" ]/2 ),
new TGeoRotation("null,",0,0,0)));
```

4.3 Software updates

Although ROOT has a pre-built element table, we decided to use exactly the same materials defined in FLUKA reading `foot.inp` file in order to achieve the best integration: for this purpose, the first task was writing a new class called `Materials`. It handles the reading of FLUKA cards and creates `TGeoMaterial` and `TGeoMixture` objects which are required by SHOE. The code works with every element and with a theoretically infinite number of elements for a single compound; it is already implemented in the present version of SHOE. As FLUKA can define compounds using atom, mass or volume fractions of single elements, the code has to manage all these cases. An example from `foot.inp` file is reported below.

```
MATERIAL                          .00120484                              AIR
COMPOUND -1.248E-4    CARBON -0.755267   NITROGEN -0.231781  OXYGEN AIR
COMPOUND -0.012827     ARGON                                             AIR
```

The second task was making the description of the geometry uniform between reconstruction and simulation. Before this work, FLUKA and SHOE did not share any input and there was a high probability of mismatching when values were modified for testing purpose. We put all input values in `foot_geo.h` file which is read by the geometry classes of tracking detectors (`TAVTparGeo`, `TAITparGeo`, `TAMSDparGeo`). Moreover, a standalone code (`MakeGeo`) reads from `foot_geo.h` and writes geometry `foot.geo` file for FLUKA and appends `ASSIGNMA` cards to material information in `foot.inp` file. Some of these cards are reported below.

```
ASSIGNMA     SILICON       VTX0       VTX3          1          1
ASSIGNMA     SILICON       ITR0       ITR1          1          1
ASSIGNMA       Epoxy    ITREPO0    ITREPO1          1          1
ASSIGNMA    ALUMINUM     ITRAL0     ITRAL3          1          1
ASSIGNMA      KAPTON    ITRCOV0    ITRCOV3          1          1
ASSIGNMA      KAPTON    ITRKAP0    ITRKAP1          1          1
ASSIGNMA     SiCFoam    ITRFOAM                     1
```

For instance, in the first card `SILICON` is the material name, `VTX0` and `VTX3` are the first and the last region made of the same material, respectively. The fifth column represents the region assignment step between `VTX0` and `VTX3`, while the last one indicates that a magnetic field is present in the region. At present, the integration between the simulation and the reconstruction framework works for tracker detectors.

Chapter 5

Study of the track reconstruction

The main goal of the FOOT experiment is to obtain the differential cross section for nuclear fragmentation at a precision level of 5%, as it is necessary for hadrontherapy purpose. To fulfill this competitive aim, the goal is to reach a momentum resolution at a level of at least 5%. In order to test and optimize the FOOT performances in momentum resolution, a set of simulated MC samples have been processed using a standard Kalman filter algorithm. At present, MC simulation with C_2H_4, C as targets and ^{12}C, ^{16}O as beams are available. In the following, a MC simulation with a 200 MeV/u ^{16}O beam impinging on a C_2H_4 target will be used. The non-uniform magnetic field of the FOOT experiment is approximated by the convolution of two gaussian distributions, each relative to a single magnet, as an approximation of a more accurate field vectorial map made on real magnets. The simulation of the materials has been carefully checked to be the same as in the simulation code for its role in the state-to-state propagation of the track during the Kalman procedure. In the first section of this chapter the basics of the momentum resolution in a magnetic spectrometer will be recalled. In the second, the track reconstruction using MC truth will be described. In the next sections, two track finding methods developed by myself and their performance will be presented.

5.1 The momentum resolution in the FOOT magnetic spectrometer

The study of the momentum resolution σ_p/p is a key task when considering a magnetic spectrometer as that in the FOOT experiment. Indeed, the momentum resolution in a magnetic spectrometer can be written as [56]:

$$\left(\frac{\sigma_p}{p}\right)^2 = \underbrace{\text{const} \cdot \left(\frac{p}{BL^2}\right)^2}_{\text{spectrometer contribution}} + \underbrace{\text{const} \cdot \left(\frac{1}{B\beta\sqrt{LX_0}}\right)^2}_{\text{Multiple Scattering contribution}} . \tag{5.1}$$

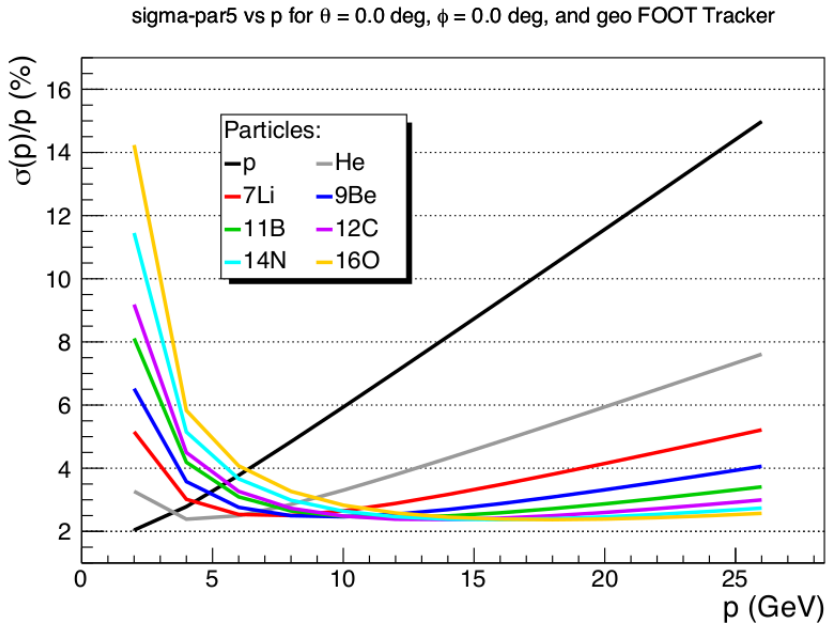

Figure 5.1: Best differential momentum resolution for a FOOT-like geometry for isotopes producing in the target.

where p is the particle momentum, B is the strength of the magnetic field, L is the length of the region where the magnetic field is present, β is the particle velocity and X_0 is the radiation lenght of the traversed material.

It is possible to predict the momentum resolution trend using an analytical calculation tool for tracking detectors: these softwares take as input the detector geometry, the sensitive elements performances and the hit density. The output of the tool developed by the PLUME collaboration [57] is reported in figure 5.1. As expected, the momentum resolution at low momentum is dominated by the MCS contribution because $\beta \ll 1$. Fixing the momentum, the resolution is larger for heavier nuclei due to the combined contribution of a lower value of β and a larger charge z.

The analytical tool presented above does not have the true FOOT geometry but only an approximation, so real performances could be different.

5.2 Study of the track reconstruction with MC truth

In order to evaluate the best performance achievable with the present FOOT setup, the first study of the track reconstruction given MC simulation was performed. This method does not know which hits belong actually to a given track because it extracts from each hit only the corresponding particle. Firstly, the SHOE software links every hit to a point of the 3D space; then, the software associates the corresponding particle to every hit

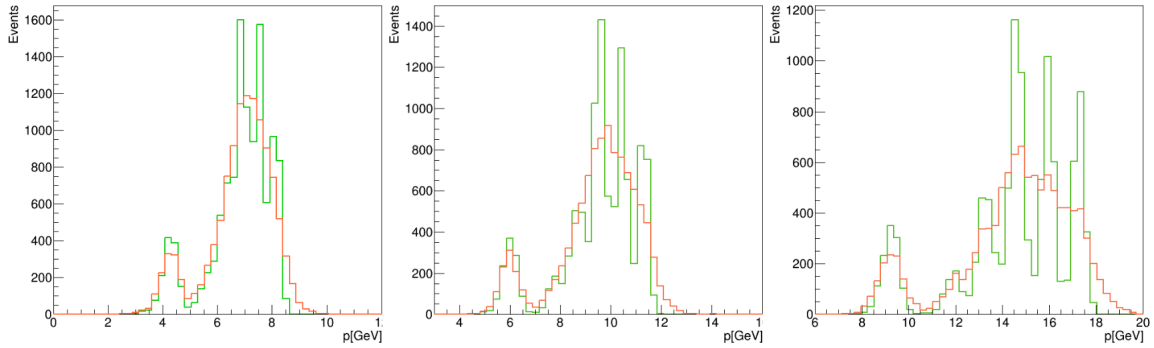

Figure 5.2: Generated (green) and reconstructed (red) momentum distribution of the considered fragments in each event for an Oxygen beam of 200 MeV/u (left), 350 MeV/u (center) and 700 MeV/u (right).

using MC data and another function fills a map which has particle names as keys and vectors of measurement as values. At present, we only accept those tracks with one hit in each layer.

Eventually, the hit collections which satisfy the requirements are fitted by the Kalman filter and the `ControlPlotsRepository` class provides a lot of useful histograms and plots. Only the main isotopes are considered: ^{6}Li, ^{8}Be, ^{9}Be, ^{10}Be, ^{9}B, ^{10}C, ^{11}C, ^{12}C and ^{12}N. The reconstruction algorithm present an efficiency $\geq 99\%$ for all the fragments of interest.

The comparison between the true generated momentum of the fragments and the corresponding reconstructed ones is reported in figure 5.2 using a simulated sample of a ^{16}O beam of 200, 350 and 700 MeV/u, hitting a C_2H_4 target. The peaks of the distribution corresponds to the different produced fragments. The global distributions of the reconstructed momenta agree with the generated ones. However, the current resolution allows to disentangle only the lighter fragments but not the heavier ones.

In order to estimate the relative momentum resolution $\sigma(p)/p$, the quantity $(p_{\text{gen}} - p_{\text{reco}})/p_{\text{gen}}$ is plotted in 200 MeV wide bins of the fragment generated momentum for every particle and fitted using a Gaussian function. Some examples for ^{12}C fragments produced by the 200 MeV/u ^{16}O beam are reported in figure 5.3. If the distribution has relative uncertainty larger than 10% or it has less than 100 entries, the momentum bin is rejected. The momentum resolution for every bin (i.e. the standard deviation of the Gaussian fit), if it satisfies these requirements, is used to fill the total momentum resolution plot. The momentum resolution as a function of the MC generated momentum is summarized in figure 5.4 for Oxygen projectiles of 200 MeV/u, 350 MeV/u and 700 MeV/u.

This preliminary momentum resolution ranges from 4.5% to 5.5%, in agreement with the goal of the experiment. As pointed out in equation 5.1, at lower momenta the resolution is limited by the Multiple Scattering in the detector materials while at higher

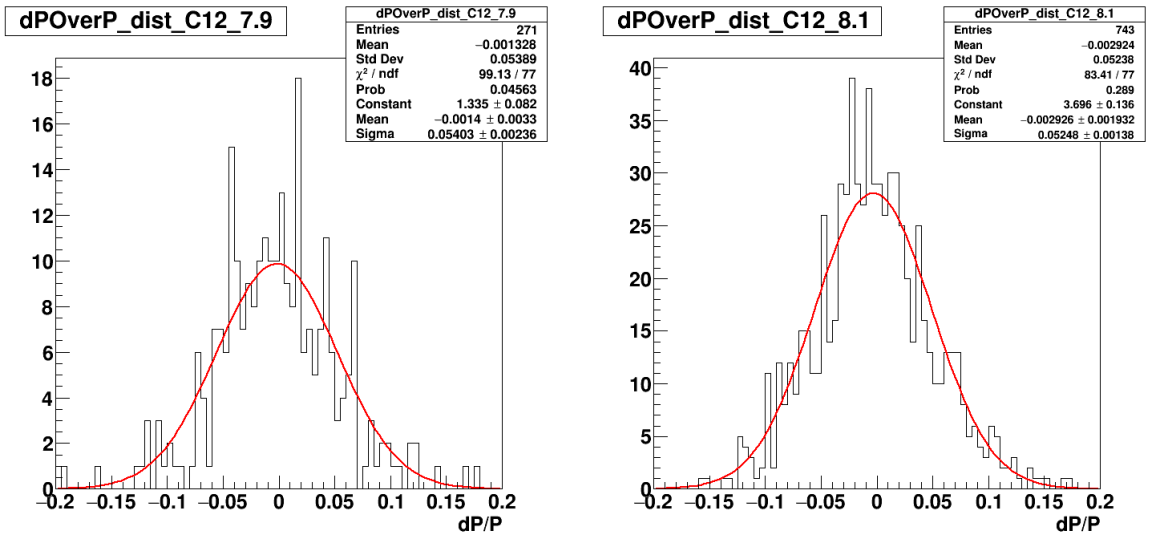

Figure 5.3: Distribution of the quantity $(p_{\text{gen}} - p_{\text{reco}})/p_{\text{gen}}$ for a ^{12}C fragment in the 200 MeV wide bin with center in 7.9 GeV/c (left) and in 8.1 GeV/c (right).

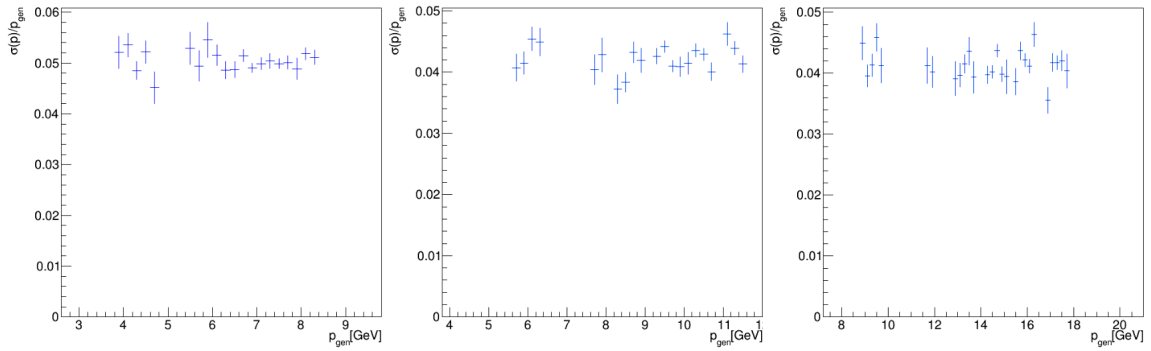

Figure 5.4: Differential momentum resolution as a function of the generated momentum for an Oxygen projectile of 200 MeV/u (left), 350 MeV/u (center) and 700 MeV/u (right).

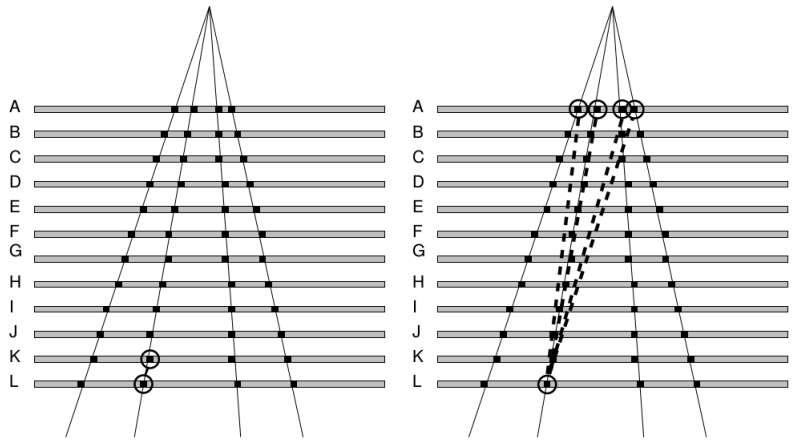

Figure 5.5: Starting tracks with nearby (left) and distant layers (right). [44].

momenta the tracking system resolution dominates.

5.3 Track finding methods

While global methods of track finding have the common property to treat all hit information in an equal and unbiased way, simultaneous consideration of all hits can be very inefficient in terms of speed. In fact many detector layouts provide sufficiently continuous measurements (such as the FOOT tracking system) so that the proximity of hits could give a hint about a track candidate. This is one of the reasons why local methods of track pattern recognition, often called *track following*, are widely used in several reconstruction programs in high energy physics [44].

Every local method of track pattern recognition needs the definition of a starting point. As illustrated in figure 5.5, it is possible to choose two different conditions: in the first case one matches hits in the neighbouring layer exploiting the minimum distance as a selection criterion. The angular precision of such a short segment is in general limited because of the small leverage, but the rate of fake track candidates is relatively small, since most wrong combinations tend to obtain a steep slope that is incompatible with the relevant physical tracks and can be discarded in the fitting step [44]. It seems to be better to start track finding from the last layer where the hit density is lower: here, the probability of mismatching is reduced with respect to vertex tracker.

A completely different approach is to combine far hits, from the first layer of the vertex tracker to the last of microstrip detector, to obtain starting points for the algorithm. These choices have potentially a much better precision in angle, but the number of combination to be considered is also much higher. The gain of precision can in fact be very limited if the material within the tracker introduces sizable multiple scattering

deflection. In the work reported in this thesis, a preliminary study of some track finding methods is performed. The results will be presented in the following.

5.4 Minimum distance method

In this track following method, hits with minimum distance between two consecutive layers are selected. It starts selecting a hit from the last layer of the tracking system (e.g. the layer L in figure 5.5) and appending the hit itself to a candidate track. The algorithm searches for hits in the next layer (e.g. the layer K) and evaluates the distance between each hit in the layer K and the hit selected in the layer L: when the loop on the layer K is finished, the hit with the minimum distance is appended to the candidate track and the algorithm moves on the next layer.

Two versions of this method are developed: one version starts from upstream (i.e. from the first layer of the vertex tracker) and the other from downstream (i.e. from the last layer of the micro strip detector). As the Kalman filter needs at least one particle hypothesis to start the prediction step, we make a guess by extracting the particle type which has generated the first hit and we pass it to the Runge Kutta extrapolator.

In order to have the same bin width and to exclude the contamination of lighter fragments in the sample, a cut on the Kalman reconstructed momentum is applied, i.e. $2.7\,\mathrm{GeV} < p_{\mathrm{reco}} < 20\,\mathrm{GeV}$. Indeed, according to MC data, this is the momentum range of interesting fragments for this study.

5.4.1 Upstream direction

As it can be seen in figure 5.6, the distributions of the reconstructed momenta agree with the generated ones. The total number of fitted tracks is obviously small if compared with the number of true tracks in the data sample: in figure 5.7, the number of fitted tracks, the number of true tracks and their ratio are reported. The ratio between the number of fitted tracks found by the considered method and the number of true tracks given by MC resembles is not a proper efficiency and it does not seem to be a good indicator for the quality of the track finding method. Thanks to the high statistics of fitted tracks with this method, it is possible to evaluate the momentum resolution which is reported in figure 5.8. Its value ranges from 5% to 6% for all fragments, not so far from the FOOT goal.

5.4.2 Downstream direction

Choosing the last layer of micro strip detector as starting point could reduce the probability of hit mismatching because the track density is lower. As it can be seen in figure 5.9, the distributions of the reconstructed momenta agree with the generated ones and this

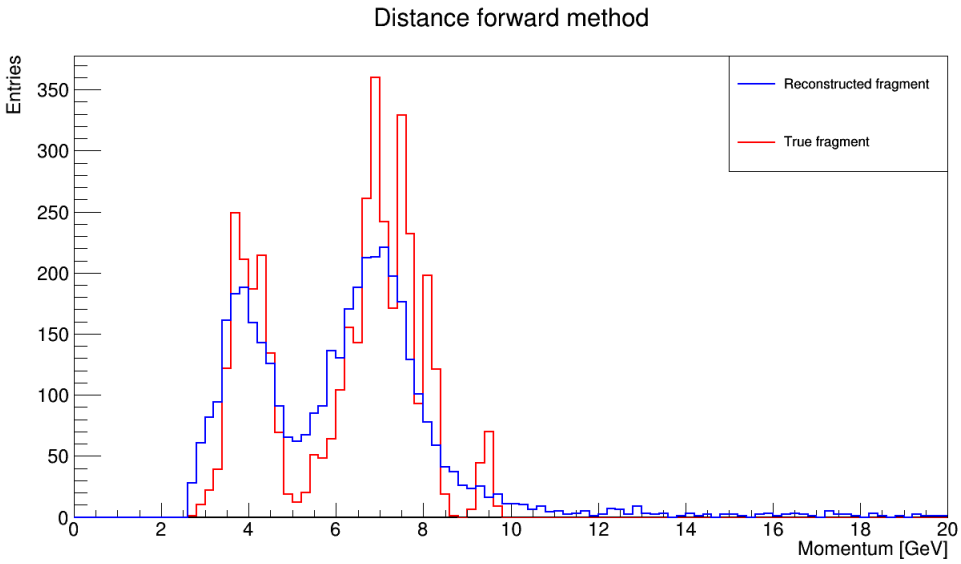

Figure 5.6: Generated (red) and reconstructed (blue) momentum distribution of the considered fragments using the minimum distance method starting from the vertex tracker.

method seems to discriminate well the peak of ^{14}N at $\simeq 9.5\,\mathrm{GeV}$. From the figure 5.10 one could claim that the downstream method is much worse with respect to the upstream one. Again, the simple ratio is not suitable to describe the features of this track pattern recognition method.

5.5 Cylinder method

In this track following method, hits which lie near a straight line are identified as a track candidate. This algorithm starts choosing a hit in the first layer of vertex tracker; this hit is combined with each hit in the last layer of the micro strip detector in a combinatorial way. The cartesian coordinates of these two hits are used to evaluate the parametric equation of a 3D straight line. Then, the intersection point between the line and each considered layer is calculated: if a hit is nearer than a certain distance (which can be set by the user, in the following 0.2 cm is used) to the intersection point, the hit is appended to the hit collection, otherwise it is rejected. If more than one hit satisfies this requirement, the nearest one is chosen. At a later time, if at least one layer does not have any hit, the whole candidate track is rejected.

For this method, only ^{7}B, ^{10}Be, ^{10}C, ^{11}C, ^{12}C and ^{14}N are considered in order to reduce the computational effort. As it can be seen in figure 5.11, the distributions of the reconstructed momenta do not agree very well with the generated ones. This method works very well in the absence of the magnetic field or when tracks have a big radius of

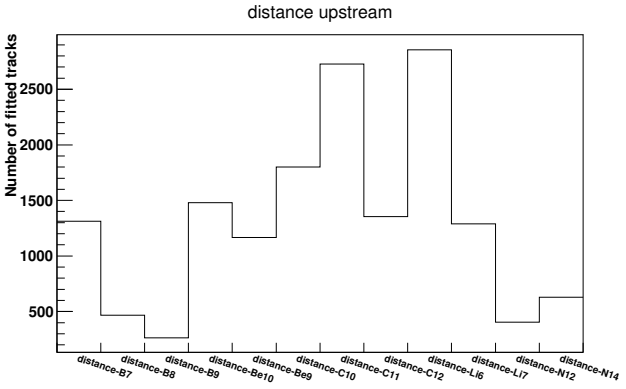

(a)

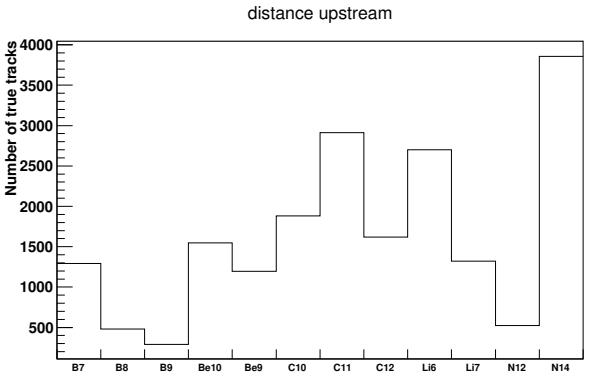

(b)

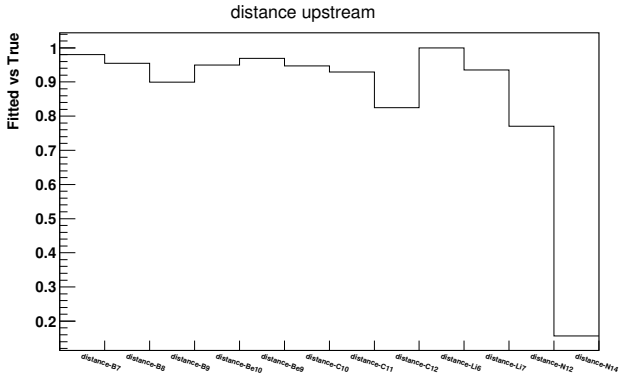

(c)

Figure 5.7: (a) Total number of fitted tracks found by upstream distance method. (b) Total number of fitted tracks given by MC truth. (c) Their ratio for upstream distance method.

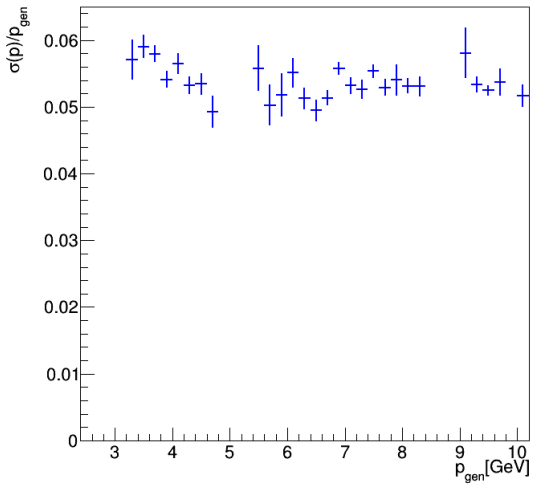

Figure 5.8: Differential momentum resolution as a function of the generated momentum for reconstructed fragments found by the minimum distance track finding method.

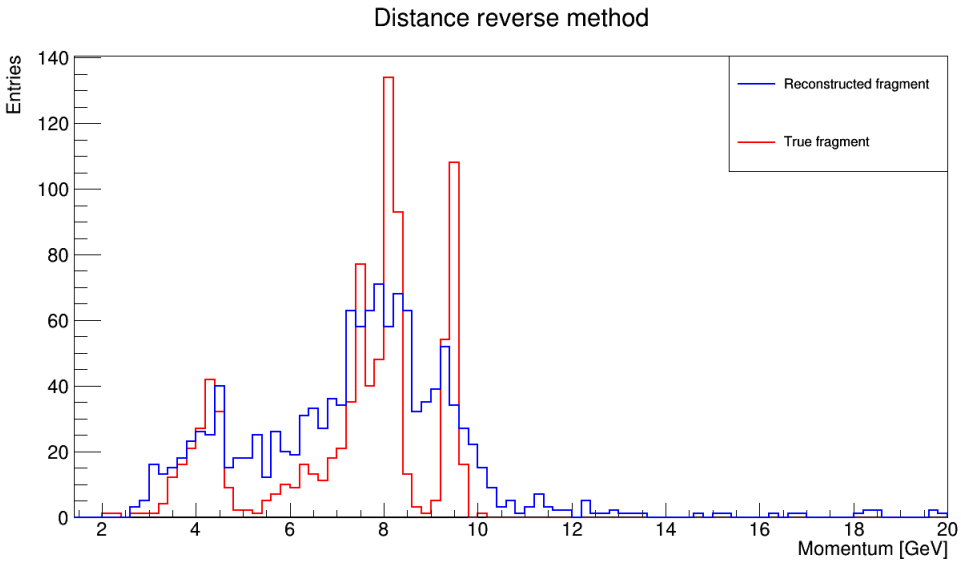

Figure 5.9: Generated (red) and reconstructed (blue) momentum distribution of the considered fragments using the minimum distance method starting from the micro strip detector.

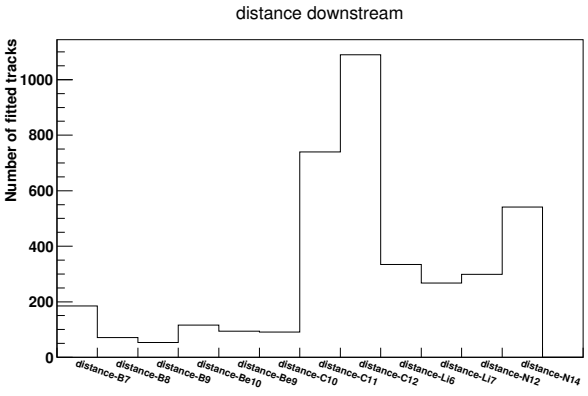

(a)

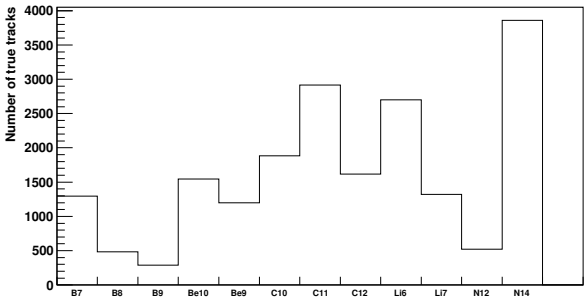

(b)

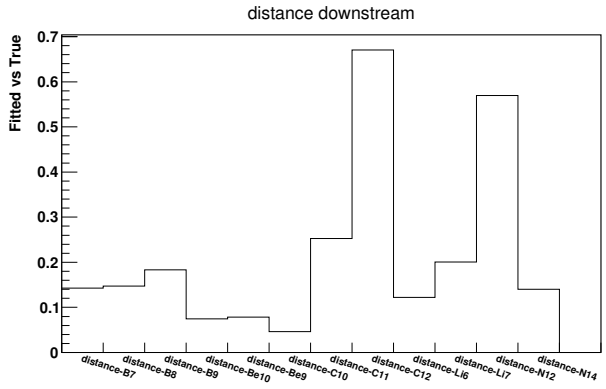

(c)

Figure 5.10: (a) Total number of fitted tracks found by downstream distance method. (b) Total number of fitted tracks given by MC truth. (c) Their ratio for downstream distance method.

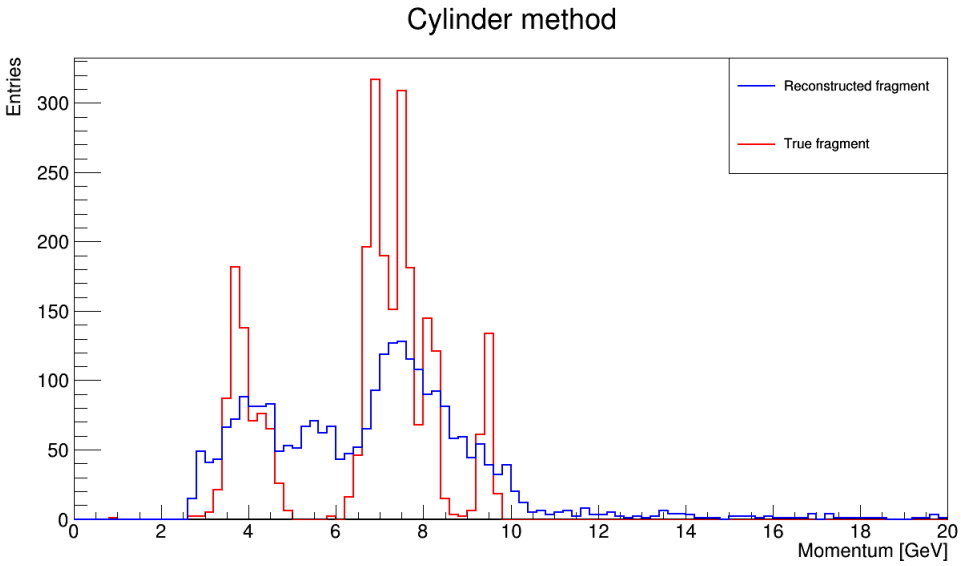

Figure 5.11: Generated (red) and reconstructed (blue) momentum distribution of the considered fragments using the cylinder method.

curvature, i.e. a high momentum and these are not FOOT conditions. Indeed, if a value of 0.1 cm for the radius of the cylinder is set, this algorithm is not able to find any track.

From figure 5.12 one can see that the efficiency for the cylinder method is the higher among the tested methods although reconstructed momenta are not well reconstructed. This is due to the combinatorial disposition of this algorithm: for each hit on the first layer, the cylinder method could associates more than one hit so that the number of fitted tracks increases. This issue can be prevented by selecting as a candidate only the track with the best χ^2 for each hit on the first layer. Unfortunately, χ^2 does not seem to be a good indicator for identified tracks in the FOOT data: the causes of such a behaviour are still under investigation.

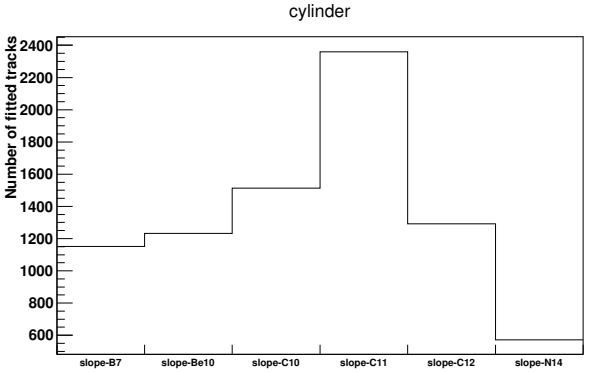

(a)

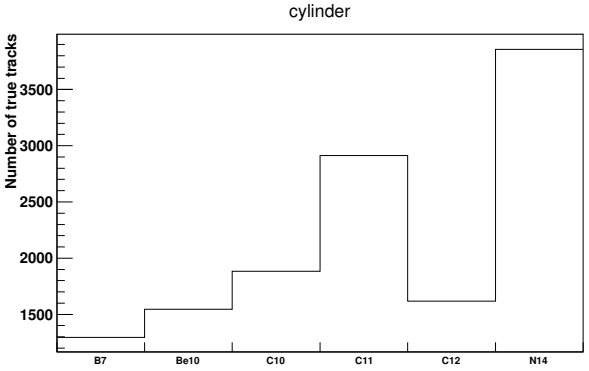

(b)

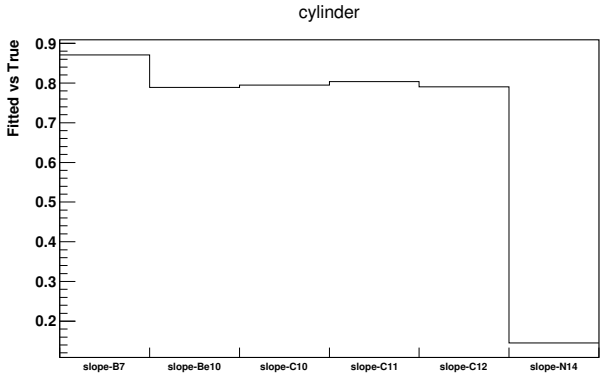

(c)

Figure 5.12: (a) Total number of fitted tracks found by cylinder method. (b) Total number of fitted tracks given by MC truth. (c) Their ratio for cylinder method.

Conclusions and perspectives

The main goal of the FOOT (FragmentatiOn Of Target) experiment is to measure the target and projectile fragmentation cross sections relevant for hadrontherapy. To achieve this goal, the FOOT experiment adopts an inverse kinematics approach to overcome the difficulties to detect fragments with a very short range ($\sim \mu$m). In order to circumvent the problems given by the presence of a pure hydrogen target, the subtraction between cross section on C and C_2H_4 is performed. The FOOT apparatus will consists of a start counter, a drift chamber acting as beam monitor, a high precision tracking system in a magnetic field, a time of flight measurement system, and a calorimeter.

The work reported in this thesis has two main goals: firstly, making uniformity between the geometries used in the simulation and the reconstruction framework, in order to avoid any compatibility problem. Before this work, the two frameworks did not share neither geometry nor material and compound information. Now all input values are put in a single file which can be read by the geometry classes of detectors; moreover, a standalone code reads from the same file to provide input for Monte Carlo (MC) simulation. Although the common geometry interface between the simulation and the reconstruction code works well for tracking detectors, it has to be extended also to other detectors such as the calorimeter. The handling of the materials and compounds defined by FLUKA already works for all detectors, instead. Despite ROOT has a pre-built element table, we decided to use exactly the same materials defined in FLUKA in order to achieve the best integration.

Secondly, we studied the performances of the track reconstruction, especially the reconstructed momenta of the fragments. Moreover, two preliminary track finding methods have been developed and compared with true hit assignments provided by MC simulation. In order to obtain the differential cross section for nuclear fragmentation at a precision level of 5%, FOOT has to achieve a momentum resolution of 5%. The study of the track reconstruction with MC truth shows that the momentum resolution with the present setup ranges from 4.5% to 5.5%, in agreement with the goal of the experiment. The reconstruction algorithm present an efficiency $\geq 99\%$ for all the fragments of interest.

Further improvements are already foreseen for the near future: firstly, a global track pattern recognition method will be tested. In global methods the whole information of

the event is used at the same time and in the same way. Global methods need a track hypothesis and they are slower than local ones; however, in the presence of a magnetic field, they should work well. The most commonly used global methods are the *Hough* transformation which is a special case of the *Radon* transformation. These algorithms do not run with the standard hit coordinates but they run in a specific *parameter space*.

Secondly, the *elastic arms* algorithm will be tested. This method is also inspired by neural networks, but works with the hits rather than with track segments. The hits are associated dynamically to templates or arms; these are parametrized track models that are fitted to the hits associated to them.

New algorithms are needed to improve the reliability, the efficiency, the speed of the track finding step thus achieving the high momentum resolution and efficient track recognition requested by the experiment.

Bibliography

[1] World Health Organization. *WHO Cancer Fact Sheet*. 2017. URL: http://www.who.int/mediacentre/factsheets/fs297/en/.

[2] American Cancer Society. *Cancer Facts & Figures 2017*. Tech. rep. American Cancer Society, 2017.

[3] International Atomic Energy Agency. *Radiotherapy in Cancer Care: Facing the Global Challenge*. Vienna: International Atomic Energy Agency, 2017. URL: http://www-pub.iaea.org/books/IAEABooks/10627/Radiotherapy-in-Cancer-Care-Facing-the-Global-Challenge.

[4] J.M. Slater. "From X-rays to Ion Beams: A Short History of Radiation Therapy". In: *Ion Beam Therapy*. Ed. by U. Linz. Springer, 2011. Chap. 1.

[5] R.R. Wilson. "Radiological use of fast protons". In: *Radiology* 47 (May 1946).

[6] Particle Therapy Co-Operative Group PTCOG. *PTCOG website*. 2017. URL: http://ptcog.ch/.

[7] International Atomic Energy Agency. *IAEA DIRAC (DIrectory of RAdiotherapy Centres)*. 2017. URL: https://dirac.iaea.org/.

[8] BNL NASA Space Radiation Laboratory. *Sito web BNL*. 2017. URL: https://www.bnl.gov/nsrl/userguide/bragg-curves-and-peaks.php.

[9] W.R. Leo. *Techniques for Nuclear and Particle Physics Experiments*. Berlin: Springer, 1987.

[10] P. Helmut. "On the Accuracy of Stopping Power Codes and Ion Ranges Used for Hadron Therapy". In: *Theory of Heavy Ion Collision Physics in Hadrontherapy*. Ed. by D. Belkic. Elsevier, 2013. Chap. 2.

[11] H.A. Bethe and J. Ashkin. "Passage of Radiations through Matter". In: *Experimental Nuclear Physics Vol.1*. Ed. by E. Segre. John Wiley, 1953. Chap. 3.

[12] National Institute of Standards and Technology (NIST). *Stopping-Power and Range Tables for Electrons, Protons, and Helium Ions*. 2017. URL: https://www.nist.gov/pml/stopping-power-range-tables-electrons-protons-and-helium-ions.

[13] W. Ulmer. "Theoretical aspects of energy-range relations, stopping power and energy straggling of protons". In: *Rad.Phys.Chem.* 76 (Feb. 2007).

[14] R. Serber. "Nuclear Reactions at High Energies". In: *Phys.Rev.* 72 (Dec. 1947).

[15] G.D. Westfall, J. Gosset, et al. "Nuclear Fireball Model for Proton Inclusive Spectra from Relativistic Heavy-Ion Collisions". In: *Phys.Rev.Lett.* 37 (Nov. 1976).

[16] K. Gunzert-Marx et al. "Secondary beam fragments produced by 200 MeV/u ^{12}C ions in water and their dose contributions in carbon ion radiotherapy". In: *New Journal of Physics* 10 (July 2008).

[17] M. Durante and F.A. Cucinotta. "Physical basis of radiation protection in space travel". In: *Rev.Mod.Phys.* 83.4 (2011), pp. 1245–1278. DOI: 10.1103/RevModPhys.83.1245.

[18] E. Haettner, I. Iwase, and D. Schardt. "Experimental fragmentation studies with ^{12}C therapy beams". In: *Rad.Prot.Dos.* 122 (Dec. 2006).

[19] L. Sihver, D. Schardt, and T. Kanai. "Depth-Dose Distributions of High-Energy Carbon, Oxygen and Neon Beams in Water". In: *Jpn.J.Med.Phys.* 18 (1998).

[20] S. Kox, A. Gamp, C. Perrin, et al. "Trends of total reaction cross sections for heavy ion collisions in the intermediate energy range". In: *Phys.Rev.C* 35 (May 1987).

[21] F. Tommasino and M. Durante. "Proton Radiobiology". In: *Cancers* 7 (Feb. 2015).

[22] A.S. Goldhaber. "Statistical Models of Fragmentation Processes". In: *Phys.Lett.* 53B (Dec. 1974).

[23] M. Giacomelli, L. Sihver, et al. "Projectilelike fragment emission angles in fragmentation reactions of light heavy ions in the energy region $<$ 200 MeV/u: modeling and simulations". In: *Phys.Rev.C* 69 (June 2004).

[24] C. Grassberger and H. Paganetti. "Elevated LET components in clinical proton beams". In: *Phys.Med.Biol.* 56 (Sept. 2011).

[25] Y. Furusawa. "Heavy-Ion Radiobiology". In: *Carbon-Ion Radiotherapy*. Ed. by H. Tsujii, T. Kamada, Shirai T., et al. Springer, 2014. Chap. 4.

[26] A. Ito, H. Nakano, et al. "Contribution of Indirect Action to Radiation-Induced Mammalian Cell Inactivation: Dependence on Photon Energy and Heavy-Ion LET". In: *Radiation Research* 165 (2006).

[27] M. Beyzadeoglu, G. Ozyigit, and C. Ebruli. *Basic Radiation Oncology*. Berlin: Springer, 2010. Chap. 2.

[28] U. Linz. "Physical and Biological Rationale for Using Ions in Therapy". In: *Ion Beam Therapy*. Ed. by U. Linz. Springer, 2011. Chap. 4.

[29] Y. Furusawa, M. Aoki, H. Itsukaichi, et al. "Inactivation of aerobic and hypoxic cells from three different cell lines by accelerated ^{3}He, ^{12}C and ^{20}Ne ion beams". In: *Radiat.Res.* 154 (2000).

[30] D. Schardt, T. Elsässer, et al. "Heavy-ion tumor therapy: Physical and radiobiological benefits". In: *Rev.Mod.Phys* 82 (2010).

[31] E.J. Hall and A.J. Giaccia. *Radiobiology for the Radiologist*. Philadelphia: LIPPINCOTT WILLIAMS and WILKINS, 2012. Chap. 7.

[32] I. Plante and F.A. Cucinotta. "Cross sections for the interactions of $1\,\mathrm{eV} - 100\,\mathrm{MeV}$ electrons in liquid water and application to Monte-Carlo simulation of HZE radiation tracks". In: *New Journal of Physics* 11 (June 2009).

[33] F. Tommasino, E. Scifoni, and M. Durante. "New Ions for Therapy". In: *International Journal of Particle Therapy* 2.3 (2015), pp. 428–438. DOI: 10.14338/IJPT-15-00027.1.

[34] The FOOT Collaboration. *FOOT Conceptual Design Report*. June 2017. URL: https://web.infn.it/f00t/index.php/en/.

[35] D. Durand, P. Sabatier, and B. Tamain. "Reaction mechanisms". In: *Nuclear Dynamics in the nucleonic regime*. Ed. by D. Durand. IoP Publishing, 2001. Chap. 5.

[36] J. Dudouet et al. "Double-differential fragmentation cross-section measurements of 95 MeV/nucleon ^{12}C beams on thin targets for hadron therapy". In: *Phys.Rev.C* 88.2 (2013). DOI: 10.1103/PhysRevC.88.024606.

[37] M. Toppi et al. "Measurement of fragmentation cross sections of ^{12}C ions on a thin gold target with the FIRST apparatus". In: *Phys.Rev.C* 93.6 (2016). DOI: 10.1103/PhysRevC.93.064601.

[38] G. De Lellis et al. "Emulsion Cloud Chamber technique to measure the fragmentation of a high-energy carbon beam". In: *Journal of Instrumentation* 2 (June 2007), p. 06004. DOI: 10.1088/1748-0221/2/06/P06004.

[39] A. Fasso' et al. "The FLUKA code: present applications and future developments". In: *ArXiv Physics e-prints* (June 2003). eprint: physics/0306162.

[40] G. Battistoni et al. "The FLUKA code: an accurate simulation Tool for Particle Therapy". In: *Frontiers in Oncology* 6.116 (2016). DOI: 10.3389/fonc.2016.00116.

[41] V. Vlachoudis. *FLUKA Advanced Interface*. 2018. URL: http://www.fluka.org/flair/.

[42] T. Böhlen et al. "The FLUKA Code: Developments and Challenges for High Energy and Medical Applications". In: *Nucl.Data Sheets* 120 (2004), pp. 211–214. DOI: 10.1016/j.nds.2014.07.049.

[43] R. Brun and F. Rademakers. "ROOT: An object oriented data analysis framework". In: *Nuclear Instruments and Methods in Physics Research A* 389 (Feb. 1997), pp. 81–86. DOI: 10.1016/S0168-9002(97)00048-X.

[44] R. Mankel. "Pattern recognition and event reconstruction in particle physics experiments". In: *Reports on Progress in Physics* 67 (Apr. 2004), pp. 553–622. DOI: 10.1088/0034-4885/67/4/R03. eprint: physics/0402039.

[45] G. Cowan. *Statistical Data Analysis*. Oxford: Oxford University Press, 1998.

[46] B.D.O. Anderson and J.B. Moore. *Optimal Filtering*. New Jersey: Prentice-Hall, 1979.

[47] K. Fujii. *Extended Kalman Filter*. URL: http://www-jlc.kek.jp/subg/offl/kaltest/.

[48] R.E. Kalman. "A New Approach to Linear Filtering and Prediction Problems". In: *Journal of Basic Engineering* 82.Series D (1960), pp. 35–45.

[49] R.E. Kalman and R.S. Bucy. "New Results in Linear Filtering and Prediction Theory". In: *Journal of Basic Engineering* 83.Series D (1961), pp. 95–108.

[50] R. Fruhwirth. "Application of Kalman filtering to track and vertex fitting". In: *Nucl. Instrum. Meth.* A262 (1987), pp. 444–450. DOI: 10.1016/0168-9002(87)90887-4.

[51] S. Fleischmann. "Track Reconstruction in the ATLAS Experiment. The Deterministic Annealing Filter". MA thesis. Bergische Univeristät Uppertal, 2006.

[52] R. Fruhwirth and A. Strandlie. "Track fitting with ambiguities and noise: A study of elastic tracking and nonlinear filters". In: *Computer Phys. Comm.* 120 (1999), pp. 197–214. DOI: 10.1016/S0010-4655(99)00231-3.

[53] M. Winkler. "A comparative study on track reconstruction methods in the context of CMS physics". MA thesis. CERN, 2002.

[54] J. Rauch and T. Schlüter. "GENFIT: a Generic Track-Fitting Toolkit". In: *Journal of Physics Conference Series*. Vol. 608. Journal of Physics Conference Series. May 2015. DOI: 10.1088/1742-6596/608/1/012042.

[55] R. Brun et al. "The ROOT geometry package". In: *Nucl.Instrum.Meth.* 502 (2003), pp. 676–680. DOI: 10.1016/S0168-9002(03)00541-2.

[56] C. Grupen and B. Shwartz. *Particle Detectors*. New York: Cambridge University Press, 2008.

[57] J. Baudot. *The PLUME project*. 2017. URL: http://www.iphc.cnrs.fr/PLUME.